

# **Studies of a Prototype Tracker for the Double Beta Decay Experiment SuperNEMO**

September 2007

James Mylroie-Smith

School of Physics and Astronomy

A dissertation submitted to the University of Manchester for the degree of master  
of Philosophy in the Faculty of Engineering and Physical Sciences

# Contents

<b>1</b>	<b>Introduction</b>	<b>14</b>
1.1	Double Beta Decay . . . . .	15
1.2	The NEMO-3 Experiment . . . . .	19
1.3	Other Previous and Current Double Beta Decay Experiments . . .	21
1.4	Next Generation Experiments . . . . .	22
1.5	The SuperNEMO Experiment . . . . .	23
<b>2</b>	<b>Physics of Geiger Cells</b>	<b>25</b>
2.1	Introduction . . . . .	25
2.2	Geiger Cell Operation . . . . .	26
2.2.1	The Gas Mixture . . . . .	29

2.2.2	Avalanche Formation and Plasma Propagation . . . . .	30
2.2.3	The Anode Signal . . . . .	31
2.3	Geiger Cell Prototypes . . . . .	33
2.3.1	NEMO-3 Cell Design . . . . .	33
2.3.2	The Single-Cell Prototype . . . . .	34
2.3.3	The 9-Cell Prototype . . . . .	36
2.4	Read-out . . . . .	38
<b>3</b>	<b>Position Reconstruction</b>	<b>40</b>
3.1	Methods for Reconstructing the Total Propagation Time . . . . .	41
3.1.1	Cathode Signals . . . . .	42
3.1.2	Anode Signals with Constant Thresholds . . . . .	42
3.1.3	Anode Signals with Sloped Thresholds . . . . .	43
3.1.4	Differentiation of the Anode Signal . . . . .	44
3.2	Longitudinal Position . . . . .	46
3.2.1	Ambiguity of the Anode Signal . . . . .	47
3.3	Position Dependence of Total Propagation Time . . . . .	49

3.3.1	Cathode Signals . . . . .	49
3.3.2	Anode Signal with Constant Thresholds . . . . .	50
3.3.3	Anode Signals with Sloped Thresholds . . . . .	51
3.3.4	Differentiation of the Anode Signal . . . . .	51
3.4	Calculating the $z$ Resolution . . . . .	52
3.4.1	Resolution from Laser Studies . . . . .	53
3.4.2	Single-cell Prototype . . . . .	53
3.5	Factors Affecting $z$ Resolution . . . . .	55
3.5.1	Cathode Resolution . . . . .	56
3.5.2	The Anode Resolution . . . . .	57
3.5.3	Atmospheric Pressure Effects . . . . .	59
3.6	Advantages of Using the Anode Signal . . . . .	61
3.7	Voltage Effects on Resolution . . . . .	61
<b>4</b>	<b>Wire Diameter Studies</b>	<b>63</b>
4.1	Introduction . . . . .	63
4.2	Simulation . . . . .	64

4.3	Single Cell Tests . . . . .	65
4.3.1	Comparison of the Signal Area with Simulation . . . . .	66
4.3.2	Resolution Comparison . . . . .	67
4.4	Results . . . . .	68
<b>5</b>	<b>Conclusion and Discussion</b>	<b>69</b>
<b>A</b>	<b>Additional Signal Properties</b>	<b>72</b>
A.1	Effects of Grounded Cathode Rings . . . . .	72
A.2	Cathode Peak Height with Hit Position . . . . .	73
A.3	Correlation Between the Anode and Cathode Signals . . . . .	74
A.4	Spikes in the anode signal . . . . .	75
	<b>Bibliography</b>	<b>75</b>

# List of Figures

1.1	Ground state masses for isobaric nuclei. . . . .	16
1.2	A schematic view of energy levels required for double beta decay.	17
1.3	Diagrams for double beta decay processes. . . . .	18
1.4	The sector layout of NEMO-3 detector. . . . .	20
1.5	A cut away view of the NEMO-3 detector. . . . .	21
1.6	A proposed design for a SuperNEMO module. . . . .	24
2.1	Ionisation which occurs as an electron passes through a cell. . . .	26
2.2	The avalanche process and propagation down the length of the cell.	27
2.3	The progression of the lead avalanche down the wire. . . . .	27
2.4	Ion pair production in helium gas over a range of voltages. . . . .	28
2.5	Illustration of the anode signal produced . . . . .	32

2.6	Typical signals from anode and cathodes. . . . .	33
2.7	A drift cell from NEMO-3. . . . .	34
2.8	The end fitting for the single-cell prototype. . . . .	35
2.9	Single-cell signal with spike from UV photon. . . . .	36
2.10	Percentage of hits with spikes seen in the signal. . . . .	37
2.11	Picture of the 9-cell prototype. . . . .	38
2.12	A signal from the 9-cell prototype. . . . .	39
3.1	The flat thresholds used in the anode signal. . . . .	43
3.2	Variable thresholds for measuring the anode signal. . . . .	44
3.3	Differentiated anode signal. . . . .	45
3.4	Total propagation time of the anode signal using the differentiat- ing method. . . . .	46
3.5	The number of hits per position found using different methods to analyse the anode signal. . . . .	48
3.6	Average total propagation times for all positions along the wire reconstructed with both cathode signals. . . . .	49

3.7	The total propagation time as a function of the fractional position is found using cathode signals. The average total propagation time found from the anode signal using constant thresholds. . . . .	50
3.8	The position dependence of the average total propagation time for both flat and variable thresholds. . . . .	51
3.9	The position dependence of the average total propagation time from sloped thresholds and differentiated signal. . . . .	52
3.10	Longitudinal resolution in Geiger cell with longitudinal position, from NEMO-3. . . . .	54
3.11	Longitudinal resolution in the single-cell prototype as a function of fractional longitudinal position. . . . .	55
3.12	Distribution of total propagation times using times from the cathodes with a Gaussian fit. . . . .	56
3.13	The distributions for the total propagation times from the anode (using flat thresholds) and the cathode signals. . . . .	58
3.14	The variation of the total propagation time with time for the anode and cathode signals. The change seen occurs over a two hour period.	60
3.15	The change in resolution with voltage. . . . .	62
4.1	Electron gain simulation over different diameters. . . . .	65



4.2	Signal area over a range of voltage with 30, 40 and 50 $\mu\text{m}$ diameter wires. . . . .	66
4.3	Resolution over a range of voltage with 30, 40 and 50 $\mu\text{m}$ diameter wires. . . . .	67
A.1	The change in cathode peak height over time. . . . .	73
A.2	The change in cathode peak height with fractional position. . . . .	74
A.3	The difference between anode and cathode times for the three different anode methods. The constant threshold method is in black, the sloped method is in blue and the differentiated method is in red. . . . .	75
A.4	The percentage of spikes over a range of voltages for anode wire diameters of 30, 40 and 50 $\mu\text{m}$ . . . . .	76

# List of Tables

3.1	Summary of the resolutions found using the four different methods. The uncertainties on $\sigma_z$ are statistical. . . . .	57
3.2	Summary of the resolutions found using the four different methods.	59
3.3	Summary of the resolutions found using the four different methods, using data from the first 900 s. . . . .	61

# Abstract

A study of the properties of drift cells operating in Geiger mode for the SuperNEMO experiment has been performed. Different methods for analysing anode and cathode signals to optimise the longitudinal ( $z$ ) resolution of the cell have been compared. The method found to be most effective is the use of constant thresholds on the differentiated anode signal. The  $z$  resolution obtained is  $(9.41 \pm 0.29)$  mm which compares to  $(10.59 \pm 0.39)$  mm from the cathode signals with  $50\text{ }\mu\text{m}$  diameter wire.

A study of the effects of changing the wire diameter was conducted. It was found that for smaller diameter wires the  $z$  resolution obtained was better. An improvement in the  $z$  resolution of  $0.7$  mm was found in changing from  $50\text{ }\mu\text{m}$  to  $30\text{ }\mu\text{m}$  wire.

These factors suggest that a drift chamber for SuperNEMO could consist of drift cells operating in Geiger mode. These cells could use single ended readout with the use of the anode and one cathode.

# Declaration

No portion of the work referred to in the dissertation has been submitted in support of an application for another degree or qualification of this or any other university or other institute of learning.

Copyright in text of this dissertation rests with the author. Copies (by any process) either in full, or of extracts, may be made only in accordance with instructions given by the author. Details may be obtained from the appropriate Graduate Office. This page must form part of any such copies made. Further copies (by any process) of copies made in accordance with such instructions may not be made without the permission (in writing) of the author.

The ownership of any intellectual property rights which may be described in this dissertation is vested in the University of Manchester, subject to any prior agreement to the contrary, and may not be made available for use by third parties without the written permission of the University, which will prescribe the terms and conditions of any such agreement.

Further information on the conditions under which disclosures and exploitation may take place is available from the Head of the School of Physics and Astronomy.

# Acknowledgements

Firstly, I would like to thank Fred Loebinger for giving me the opportunity to study in Manchester. I would also like to thank my supervisor, Stefan Söldner-Rembold, for the help and advice he has given me over the past year. My thanks must also go to Steve Snow and Irina Nasteva for their constant help advice and support. A big thank you must also go to Ray Thompson, Julian Freestone and Andy Elvin for all their work constructing the prototypes and helping me with any problems.

An especially big thanks to my NEMO/SuperNEMO office mates who I can't imagine the year without. To the members of the badminton, squash and football clubs thank you for the good times. Also to all the members of the Department who have made it such a welcoming and enjoyable place to work over the last year, thank you.

To all my family thank you for your support through the course of the year, you have all been great.

# Chapter 1

## Introduction

This thesis describes the research on the design of drift cells operated in Geiger mode (Geiger cells), for use in the proposed SuperNEMO experiment. Geiger cells have previously been used in a high energy gamma ray astronomy experiment called HEGRA which ran until 2002 [1]. Currently they are being used in the double beta decay experiment NEMO-3 [2]. They provide a cheap and effective method of tracking charged particles. The proposed SuperNEMO experiment would again utilise Geiger cells to provide tracking.

The aim was to optimise performance for use in the SuperNEMO experiment. New methods for reconstructing the particle position from the arrival times of anode signals in Geiger cells have been developed. The resolution of the cell found using this new method has been compared to the resolution found using established methods. A comparison of resolution with 30, 40 and 50  $\mu\text{m}$  wire diameters has also been made.

## 1.1 Double Beta Decay

The process of double beta decay is the focus of the NEMO-3 experiment. The SuperNEMO experiment aims to extend the reach of NEMO-3 and place tighter constraints on the properties of neutrinos. This chapter discusses what information double beta decay gives about the neutrino. It examines the way previous and current experiments have searched for double beta decay.

Figure 1.1 shows the ground state masses for isobaric nuclei. The two parabolas show even-even and odd-odd states. The splitting of these states originates from the nuclear pairing energy acting between identical nucleons. Transitions between the different isotopes can occur through single beta decay and double beta decay. Single beta decay is only possible between certain isotopes. In some cases it is forbidden or highly suppressed, by mass constraints or the requirement of large spin changes. Double beta decay can only be studied in the case where single beta decay is not allowed, because the single beta decays have much shorter lifetimes than double beta decays [3]. A schematic picture of the requirements for observable double beta decay is shown in Figure 1.2.

Double beta decay is a nuclear process which is the simultaneous beta decay of two neutrons in the same nucleus. Double beta decay can be described by a second order perturbative expansion of the weak interaction. The higher order nature of the decay results in long lifetimes of typically  $10^{20}$  years. Double beta decay was first proposed by M. Goeppert-Mayer [5] in 1935. Double beta decay is characterised as a process which increases the nuclear charge ( $Z$ ) by two units while the atomic

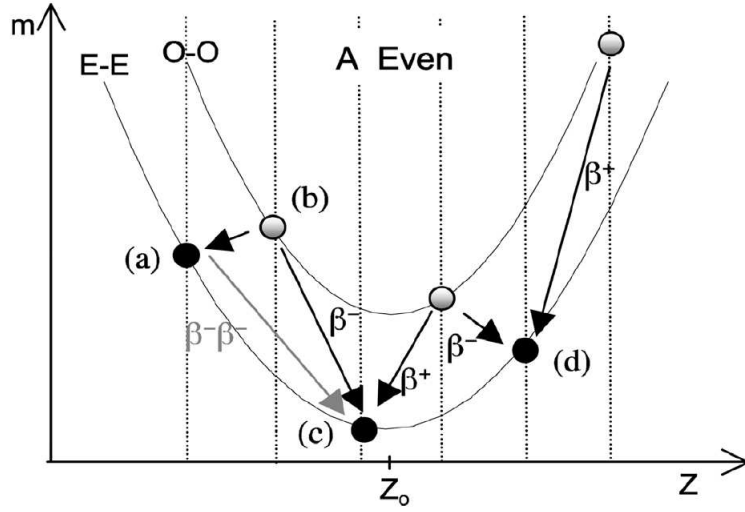


Figure 1.1: Ground state masses for isobaric nuclei [4].

mass remains the same ( $A$ ).

$$(Z, A) \rightarrow (Z + 2, A) + 2e^- + 2\bar{\nu}_e \quad (1.1)$$

Double beta decay can only occur in even-even nuclei. All even-even nuclei have ground states of spin 0 and positive parity. To allow double beta decay it is required that the mass  $m(Z, A)$  is greater than  $m(Z+2, A)$  [4]. There are 35 known double beta decay isotopes.

Another process of double beta decay was later described by Furry [6]. This neutrinoless process violates lepton number.

$$(Z, A) \rightarrow (Z + 2, A) + 2e^- \quad (1.2)$$

For neutrinoless double beta decay to occur a massive Majorana neutrino is required [4]. Figure 1.3 shows the processes of double beta decay and neutrinoless



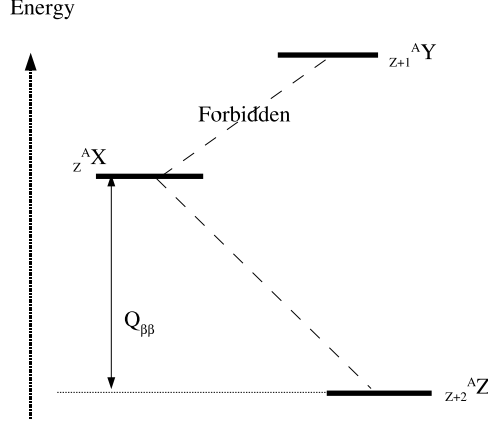


Figure 1.2: The atomic energy levels required to observe double beta decay ( $^A_Z X \rightarrow ^A_{Z+2} Z$ ).

double beta decay. Neutrinoless double beta decay can only proceed if neutrino and anti-neutrino are identical and if there is helicity matching through the process. A massive Majorana neutrino fulfils both of these conditions.

Neutrinoless double beta decay is of particular interest. It gives both a measurement of the effective neutrino mass and insight into the fundamental nature of the neutrino (Majorana or Dirac). A Dirac particle is one whose particle and anti-particle can be distinguished. A Majorana particle is one whose particle and anti-particle are indistinguishable. The half-life of neutrinoless double beta decay  $T_{1/2}^{0\nu}$  is connected to the effective neutrino mass  $\langle m_{\nu_e} \rangle$  :

$$(T_{1/2}^{0\nu})^{-1} = G^{0\nu} |M^{0\nu}|^2 \left( \frac{\langle m_{\nu_e} \rangle}{m_e} \right)^2, \quad (1.3)$$

where  $G^{0\nu}$  is the phase space factor and  $M^{0\nu}$  is the nuclear matrix element. The phase space factor is calculated and has only small uncertainties in its value. The

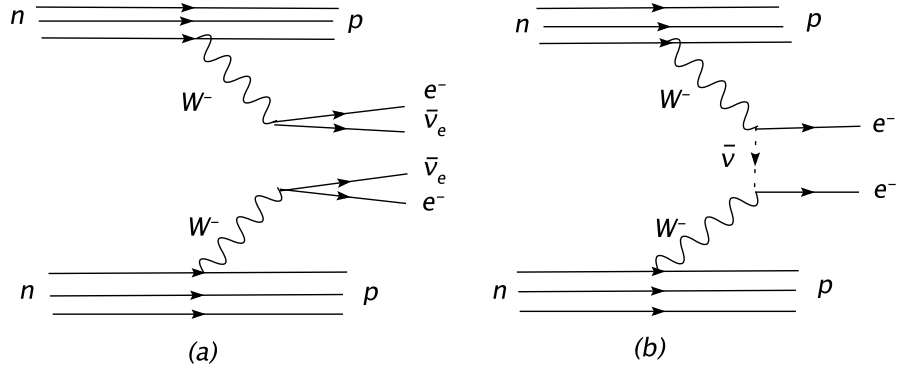


Figure 1.3: Diagrams for double beta decay processes: a) two-neutrino double beta decay, b) neutrinoless double beta decay.

nuclear matrix element is derived from a nuclear model with uncertainties which give a large systematic uncertainty in the value of  $m_{\nu_e}$  [3].

Double beta decays are studied by a variety of different experiments. There are three methods to study double beta decay: geochemical, radiochemical and direct. Only the direct method is sensitive to the neutrinoless decay mode. NEMO-3 and CUORICINO are two currently running experiments which use the direct method.

In tracking plus calorimeter experiments, such as NEMO-3, the electron tracks and their energies are measured separately. The tracking plus calorimeter technique used in NEMO-3 allows electron/photon separation and the measurement of the angular distribution of the double beta decay events. This cannot be performed in experiments which use a “source=detector” method. Source detector experiments use a double beta decay isotope as both the source and detector. These experiments benefit from a good energy resolution but have difficulties understanding background signals.

## 1.2 The NEMO-3 Experiment

The Neutrino Ettore Majorana Observatory 3 (NEMO-3) is a double beta decay experiment. It is located in the Fréjus underground laboratory. It uses a tracking plus calorimeter technique to study the double beta decay processes of several isotopes.

The NEMO-3 detector consists of 20 identical sectors which form a cylindrical shape. The sectors each contain foils made from double beta decay isotopes. The NEMO-3 detector houses about 10 kg of double beta decay isotopes. The largest contribution to this comes from  $^{100}\text{Mo}$  (6.9 kg) and  $^{82}\text{Se}$  (0.93 kg). One of the benefits of the NEMO-3 detector is its ability to examine the double beta decay processes in a variety of isotopes.

The total tracking volume contains 6180 drift cells which provide three-dimensional track reconstruction. Each cell is 2.7 m in length and 28 mm in diameter. The drift cells are operated in Geiger mode and use a gas mixture of helium (99%), argon (1%), ethyl alcohol (40 mbar partial pressure) and water (1500 ppm). The drift cells are arranged in layers forming a “4-2-3” configuration and have a 138 mm gap between each layer. The layout of a sector can be seen in Figure 1.4. The layer of 4 cells close to the foil gives precise vertex reconstruction and provides identification of  $\alpha$  particles. The layers of 2 and 3 cells give precise measurement of the curvature of the tracks. Allowing separation between charged and neutral particles.

Between the layers on the top and bottom there are scintillators with low radiation

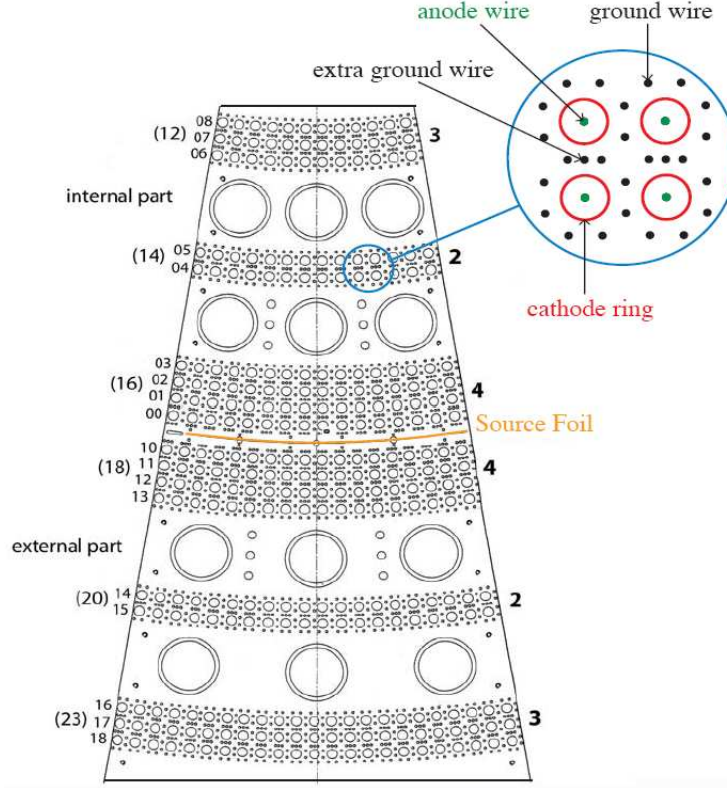


Figure 1.4: The sector layout of NEMO-3 detector [2].

PMTs. Scintillators also surround the tracking volume and provide information on the time of flight and the energy of the particles.

The whole tracking volume is contained within a solenoid which provides a 25 Gauss magnetic field used to identify the charge of particles. This field helps to eliminate background from crossing electrons by identifying electrons and positrons through their track curvature. The layout of the NEMO-3 detector is shown in Figure 1.5.

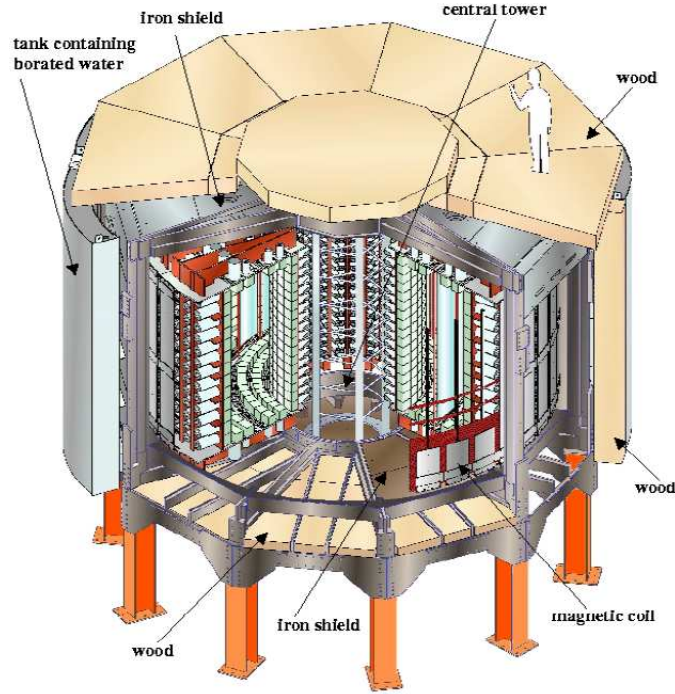


Figure 1.5: A cut away view of the NEMO-3 detector [2].

### 1.3 Other Previous and Current Double Beta Decay Experiments

The Heidelberg-Moscow experiment which ran from 1990 to 2003 used 11 kg of high purity Ge-detectors to measure double beta decay. Initially the group reported no signal for neutrinoless decay placing a half-life limit for the process [7]:

$$T_{1/2}^{0\nu}({}^{76}\text{Ge}) > 1.9 \times 10^{25} \text{ y} \quad (90\% \text{ CL}), \quad (1.4)$$

corresponding to a neutrino mass smaller than 0.35 eV. The results were subsequently reevaluated by a subgroup of the collaboration. They reported a peak in

the data consistent with a neutrino mass of 0.2-0.6 eV [8].

IGEX is a “source-detector” experiment which ran at the Canfranc underground laboratory [9]. It used three 2 kg high-purity Ge detectors enriched to 86% with  $^{76}\text{Ge}$ . These were contained within low background shielding and used techniques to separate single-site events from multi-site events. Single-site events are events that originate from one point in the detector. They obtained a similar limit on  $^{76}\text{Ge}$  to the Heidelberg-Moscow experiment .

CUORICINO is currently running at Gran Sasso Underground Laboratory in Italy. It uses bolometers running at very low temperatures (mK). Double beta decays deposit enough energy to create a temperature change which is detectable. It contains 40 kg of  $\text{TeO}_2$  crystals to search for the decay of  $^{130}\text{Te}$ . The recent result from CUORICINO is the limit:

$$T_{1/2}^{0\nu}(^{130}\text{Te}) > 3 \times 10^{24} \text{ y} \quad (90\% \text{ CL}), \quad (1.5)$$

giving a neutrino mass of smaller than 0.2-0.98 eV [10].

## 1.4 Next Generation Experiments

COBRA, GERDA and SuperNEMO are three next generation double beta decay experiments. COBRA is a source equals detector experiment and will use a large array of CdZnTe semiconductor crystals. These crystals contain nine double beta decay isotopes and will benefit from the good energy resolution of the semiconductors. Currently measurements have been made using four  $1 \text{ cm}^3$  CdZnTe

detectors. This is being extended to a 64 detector array and there are plans for a 60,000 array.

GERDA is another source equals detector experiment. It is a high-purity germanium detector (HPG) using segmented detectors and analysis of the detector response function have been used to give greater background rejection.

## **1.5 The SuperNEMO Experiment**

SuperNEMO will use many of the same techniques and incorporate many of the lessons learned from NEMO-3 to improve the range of neutrino masses probed. It will contain a total of 100 kg of double beta decay isotopes consisting mostly of  $^{82}\text{Se}$  and  $^{150}\text{Nd}$ . The concept for SuperNEMO is to use 20 individual modules. Each module will consist of around 3000 Geiger cells surrounded by walls of scintillators.

The modular construction allows a combination of different double beta decay isotopes to be studied. By optimising the resolution from the Geiger cells an improved background rejection can be achieved. Figure 1.6 shows the proposed layout for the SuperNEMO modules.

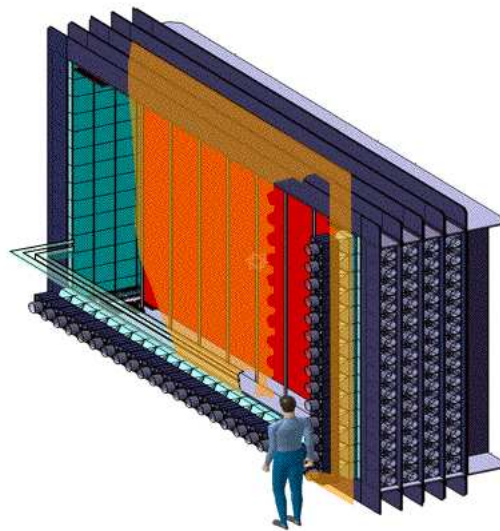
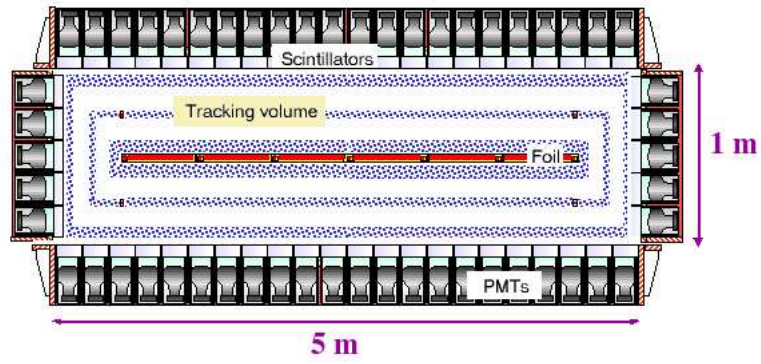


Figure 1.6: A proposed design for a SuperNEMO module.



# Chapter 2

## Physics of Geiger Cells

### 2.1 Introduction

This chapter describes the properties of a Geiger cell and the characteristics of the signal induced by a charged particle passing through the cell. Geiger cells are wire drift chambers which operate at high voltages. At these voltages an initial ionising particle triggers an avalanche effect which provides noise-free amplification.

The resulting signal provides information about the position of the initial ionisation event. Unlike proportional chambers, there is no information about the energy of the initial ionisation event. One limitation of Geiger cells is the large dead time they experience due to the time it takes for the field to recover after ion collection. This is not a problem for experiments such as SuperNEMO and NEMO-3 owing to their low event rates ( $\sim 0.2$  Hz).

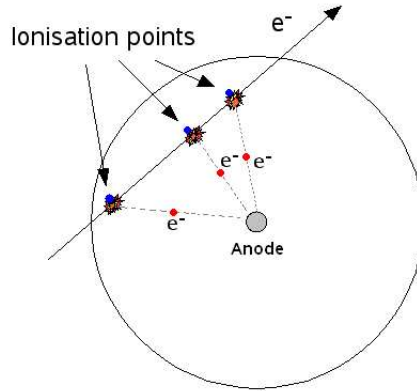


Figure 2.1: Ionisation which occurs as an electron passes through a cell.

## 2.2 Geiger Cell Operation

The wire cells that have been studied consist of a ring of ground wires with one central anode wire and a copper cathode ring at each end. The system is immersed in a gas mixture of helium, argon and alcohol. Charged particles ionise the gas as they pass through the cell. Typically there are multiple ionisations inside a cell. Figure 2.1 is a diagram of an electron passing through the cell. As the electrons traverse the cell, they approach the anode wire and start to ionise more of the gas starting an avalanche process. This avalanche process becomes significant in the region very close (within  $\sim 1$  mm) to the wire. The avalanche creates photons which travel further along the wire and initiate new avalanches. This process is shown in Figure 2.2. Some of the long range photons can reach the edges of the cell. The avalanches create “burn” regions as the process progresses along the length of the anode wire (see Figure 2.3). The act of these travelling the length of the wire creates a current on the wire.

The high voltage applied to the anode wire changes the mode of operation of the

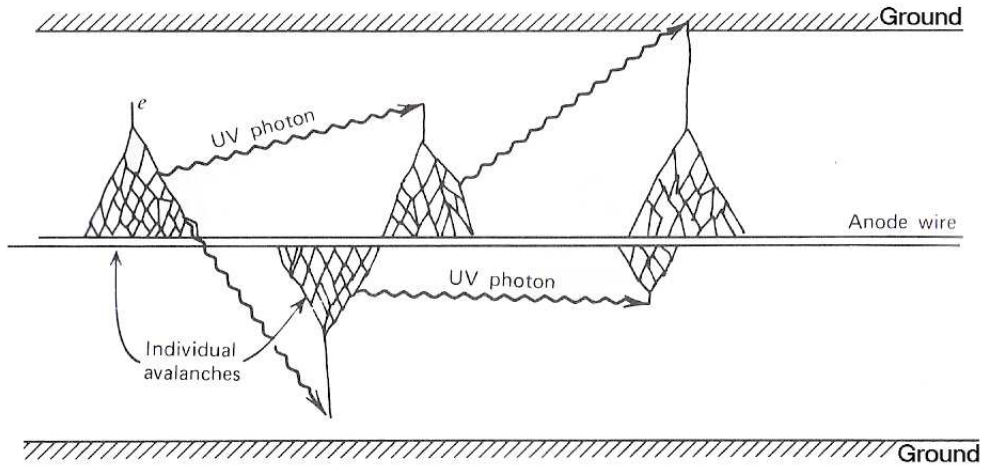


Figure 2.2: The avalanche process showing the method of propagation down the length of the cell [11].



Figure 2.3: The progression of the lead avalanche down the wire.

cell. At high voltages the cell enters a region of operation known as the Geiger mode. Figure 2.4 shows the counting rate of a Geiger cell as a function of voltage [11]. The points of operation considered here are within the Geiger plateau. In the higher range of voltages problems arise due to self-triggered discharges that can result in the cell constantly firing. At the lower end of the plateau, problems arise due to the signal failing to propagate the full length of the wire. In these instances an incorrect position is reconstructed. Once the voltage drops enough the cell re-enters proportional mode.

There are large differences between proportional and Geiger mode. One of the most crucial differences is that in the Geiger mode of operation, the cell does not

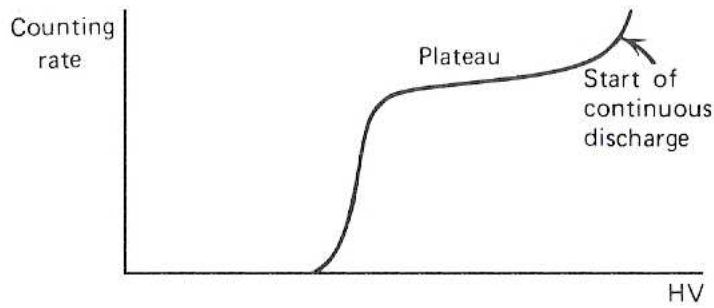


Figure 2.4: Ion pair production in helium gas over a range of voltages.

keep any of the information concerning the initial energy of the ionising particle. This is because the different mechanisms through which the gas multiplies the signal result in a large difference in the number of electrons produced. In proportional mode the gas multiplication factor is  $10^2 - 10^4$ , depending on the energy of the initial particle. In Geiger mode the number of electrons produced is independent of the initial particle energy. It depends only on the voltage applied to the wire. The difference in the signals results in different requirements from the readout electronics. For the Geiger operation simple RC circuitry can be used, whereas for the proportional mode far more sophisticated circuitry is required.

Geiger cells have several features which allow their use in low energy particle physics. They can be made with low radioactivity materials and require very little material. This keeps their background low. They are cheap and therefore their use over large volumes is possible. The main drawback for Geiger cells is their long dead times, which prevents their use in many accelerator experiments. This is not a problem for low count rate experiments such as NEMO-3.

### 2.2.1 The Gas Mixture

The gas used is a mixture of helium (95%), argon (1%) and alcohol (4%). The two noble gases comprise the majority of the fill gas of the cells. The use of helium with low  $Z$  minimises the energy lost by the charged particles to the gas. When a charged particle crosses the cell it ionises the gas at several points. The electrons and ions then drift toward the anode and cathode wires respectively. When an ion reaches the cathode wire there is a small probability that during the process of neutralising the ion will create another free electron. This electron would then initiate another avalanche. This multiple pulsing effect increases as the voltage is increased until reaching a point of continuous discharge.

There are several different methods to quench the Geiger cells. This can be done with the use of external quenching, which can take the form of reducing the voltage after a fixed time and this generally has to last for a few  $100\ \mu\text{s}$  [11]. More often internal quenching is used and this is accomplished by a quenching gas. Alcohol is added as such a quenching agent. The quenching gas is chosen to have a lower ionisation potential and a more complex molecular structure than the helium and argon. The quenching agent is added in concentrations of typically 5–10%. The quenching gas affects the drifting ions, which are mostly from the fill gas. As the ions drift toward the cathode wires they collide with the quenching gas molecules. Due to the lower ionisation potential of the quench gas molecules they are ionised. The result is that all the ions arriving at the cathode are those of the quenching gas. These more complex molecules are less likely to create free electrons. The addition of the quenching gas also extends the Geiger plateau making the cell operation stable over a larger range of voltages [11].

### **2.2.2 Avalanche Formation and Plasma Propagation**

Geiger cells operate with large electric fields on the anode wire. In these strong fields electrons excited from the atoms in the gas create an avalanche which excites more and more electrons and ions. Many of the ions produced emit photons which in turn excite more electrons further along the wire. It is through these photons that the discharge propagates along the length of the wire.

The ions and electrons created by the initial charged particle are attracted toward the cathodes and anode, respectively. The electrons move very quickly compared to the ions. As they approach the anode wire they produce more ionisation and the number of electrons grows quickly. This region close to the wire plays an important role in the avalanche growth and the plasma propagation. The time for the electrons to travel from the closest ionisation point to the wire is used to specify the circumference along whose tangent the particle passed.

Typically there are of the order  $10^6$  electrons produced as the electrons approach the central wire. The slow moving ions can be considered stationary relative to the electrons. While the number of ions increases, they start to build up charge and affect the electric field near the anode. With the reduced field the electrons gain less energy and this in turn reduces the overall number of electrons being produced. When the ion charge cancels enough field so that the electrons no longer multiply, the avalanche is broken off. This effect is local to the region of wire where the ionising particle passed. The areas surrounding the avalanche still maintain their original field.

It is in these surrounding regions that the mode of plasma propagation begins. As

the avalanche develops it also spreads into these regions. The plasma progresses through the emission of long range UV photons which trigger avalanches further along the wire. The method by which the ions progress is voltage dependent. At lower voltages their propagation is more irregular and contains more regions of localised burning with subsequent burning further along the wire. At the higher voltages this process becomes smoother. The propagation velocity becomes constant over the whole length of the wire. Burning continues till the plasma reaches the ends of the wire. There it encounters the cathode rings which create a stronger field and a more intense plasma as it propagates through them.

### **2.2.3 The Anode Signal**

The avalanche followed by plasma propagation produces signals on both the anode wire and the cathode rings. The signal generated on the anode wire takes the form shown in Figure 2.5. When the plasma is formed it travels out from the original point in both directions. As the plasma progresses along the wire, charge is added at a constant rate, shown as region 2 in the figure. When the signal reaches one end of the wire the charge generated is approximately halved (point 3) as the plasma propagates in only one direction (region 4). When the second end is reached the charging effect stops and the signal finishes.

A typical anode signal, recorded with an oscilloscope, is shown in Figure 2.6. The anode signal has a small gradient in the flat regions as the plasma propagates. This gradient arises because of the RC circuit used. Using different RC circuits changes the gradient of this slope.

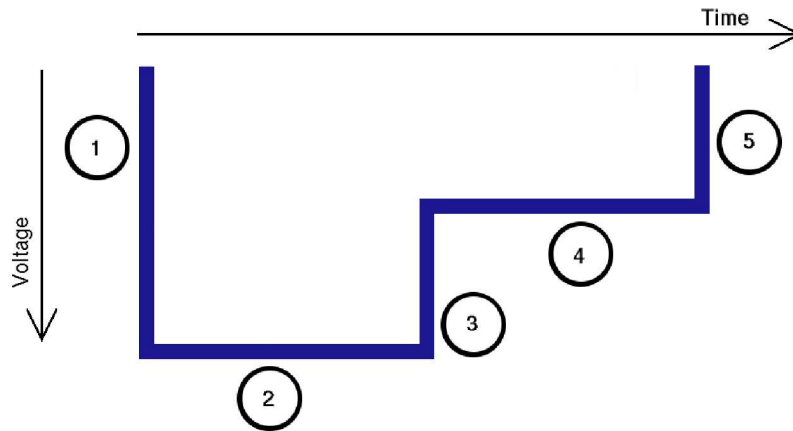


Figure 2.5: The signal generated on the anode by the plasma. 1) initial avalanche, 2) plasma propagating in both directions, 3) plasma reaches one end of wire, 4) plasma propagating in one direction, 5) plasma reaches other end of wire.

The cathode ring signals arise when the plasma reaches inside the ring. When the plasma reaches the increased field strength of the rings, this creates a sudden increase in the anode signal (a spike) and also the signals seen in the cathodes. The cathode signals are a result of the charge ions near the anode wire moving toward the cathode ring. Due to the intensity of the field close to the wire even very small movement toward the wire creates a large change in the field on the cathode ring. The following chapter examines the use of these signals, in determining the propagation time and position which this translates to.

When the plasma reaches the end of the wire and enters the cathode ring, the field which it experiences increases significantly. This is due to the difference in the electrostatics between the ring of ground wires and the solid copper ring of a smaller diameter. This change in field creates an increase in the size of the plasma that would propagate. This creates a rapid increase in the plasma size and creates a spike in the anode signal.



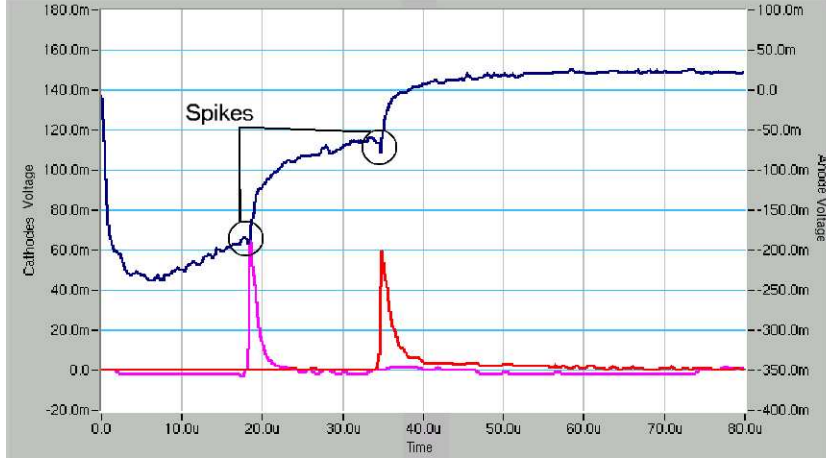


Figure 2.6: A typical single-cell anode signal in blue, typical cathode signals in red and pink.

## 2.3 Geiger Cell Prototypes

Several prototypes were constructed to study the signal properties. The design of these prototypes is based on the NEMO-3 cell design.

### 2.3.1 NEMO-3 Cell Design

In NEMO-3 the  $z$  position is reconstructed using the initial drift time of the electrons and the two cathode signal times. A NEMO-3 drift cell consists of a ring of 8 or 10 ground wires surrounding a central anode wire. The wires have a diameter of  $50\text{ }\mu\text{m}$  and are made from stainless steel. The only difference between the anode wire and the ground wires is that the anode wire has been cleaned with heptane and then baked at  $650^\circ\text{C}$ . The aim of this baking was to remove impurities from the surface as these can lead to problems with the plasma propagation and prevent the correct functioning of the cell.

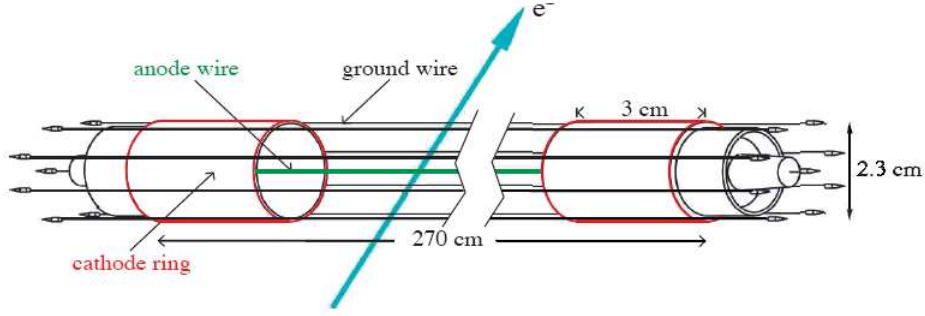


Figure 2.7: A drift cell from NEMO-3.

At each end of the wire there are 30 mm long copper cathode rings with a diameter of 23 mm. The cathode rings are grounded and create a more intense field at the ends of the cell. Their signals are read out with the use of simple electronics to give the times the plasma reaches the ends. The longitudinal position at which the charged particle crossed the chamber can then be reconstructed. A diagram of a NEMO-3 cell can be seen in Figure 2.7.

To understand the advantages and disadvantages of the various methods, for reconstructing the position in the cells, two different prototypes were used, a single drift cell and a 9-cell prototype. These cells are described and their properties explained in Sections 2.3.2 and 2.3.3.

### 2.3.2 The Single-Cell Prototype

A single-cell prototype was constructed to measure plasma propagation along the anode wire. The cell consists of a 3020 mm long copper tube with a single stainless steel anode wire inside. In this case the copper tube acts as the ground and this creates a simple electrostatic system to examine. It is also possible to investi-

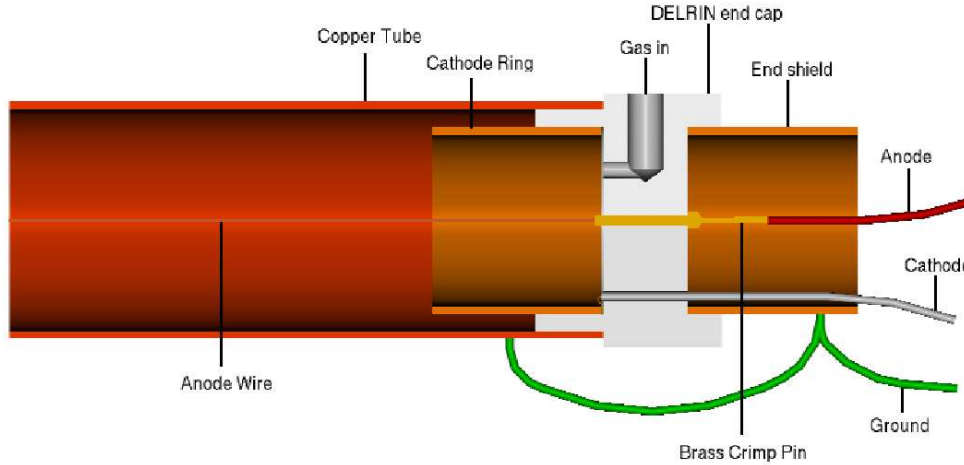


Figure 2.8: The end fitting for the single-cell prototype.

gate the changes which occur when using different wire diameters. At the ends of the cell there are cathode rings and the cell is filled with a gas mixture of helium (95%), argon (1%) and ethanol (4%). A drawing of the cell end fittings is shown in Figure 2.8.

Due to the specific cell configuration there are some features of the anode signal which are unique to the single-cell prototype. One of them is the emergence of spikes on the anode signal. An example of the spikes can be seen in Figure 2.9. These are caused by long-range UV photons which travel further along the length of the wire than the plasma. Once ahead of the plasma they can excite an electron from the copper tube which begins another avalanche. From this avalanche a second plasma starts to propagate in both directions. When it meets the original plasma it stops propagating in that direction and the other direction becomes the front of the plasma. As a result of the long range UV photons the plasma has a shorter total propagation time. This effect is not seen in wire setups, such as NEMO-3, as there are only a small number of collisions with the wire surfaces.

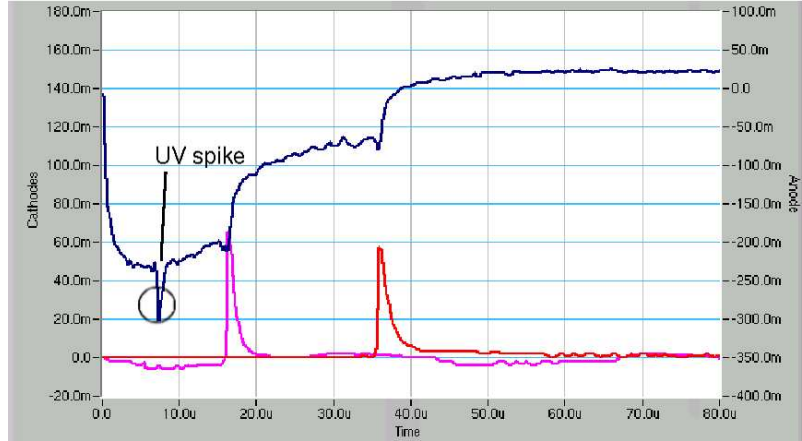


Figure 2.9: A signal from the single-cell prototype with a spike on the anode signal (top) produced by long range UV photons.

Signals with such spikes occur in about 16% of the cases for the single-cell, these were excluded from the analysis.

The percentage of events which contain spikes increases with voltage. Figure 2.10 shows how the percentage of spikes increases with voltage. The spike percentage relates to the number of UV photons produced which can reach the walls of the cell.

### 2.3.3 The 9-Cell Prototype

The 9-cell prototype consists of nine NEMO-3 like cells. Each cell is 1.8 m long and consists of a anode wire surrounded by 12 ground wires. They all have 30 mm grounded copper cathode rings. They are assembled in a square 3×3 configuration. A picture of the wired cells is shown in Figure 2.11. The 9-cell prototype is supplied with the same gas as the single-cell prototype. Because the cells use

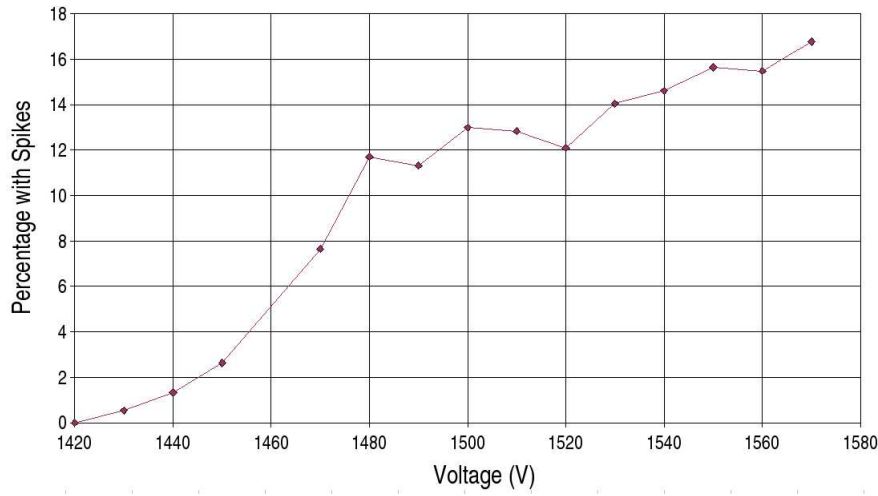


Figure 2.10: Percentage of hits with spikes seen in the signal.

ground wires, the UV spikes are no longer present in the anode signals.

The signals are different to those from the single cell because the cathode rings now have a much greater effect. This produces much larger signals in the cathodes and also creates spikes in the anode signals. The increase in the signal size seen on the anode comes from the greater change in the electrostatics as the plasma enters the cathode ring. The longer cathode rings used in this set up also increase the size of the cathode signals. The resulting signals can be seen in Figure 2.12. A cross-talk effect can be seen on the cathode signals, due to the neighbouring cathode rings firing. It requires the cathode signal thresholds to be set high ( $\sim 150$  mV) to suppress this effect.

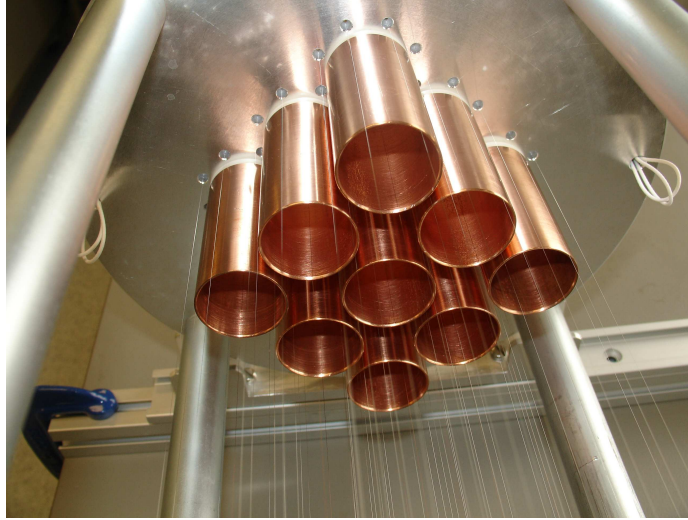


Figure 2.11: The 9-cell prototype with copper cathode rings and wires.

## 2.4 Read-out

The signals from the anode wire and the two cathodes were read using two oscilloscopes. They were triggered off cosmic rays, either with the use of scintillators, or directly from the anode signals. A system was developed which used LabVIEW to digitise and store data from four channels of oscilloscopes. A separate LabVIEW program was subsequently used to analyse the stored data. The analysed data were converted to ROOT [12] files which could then be used for further analysis.

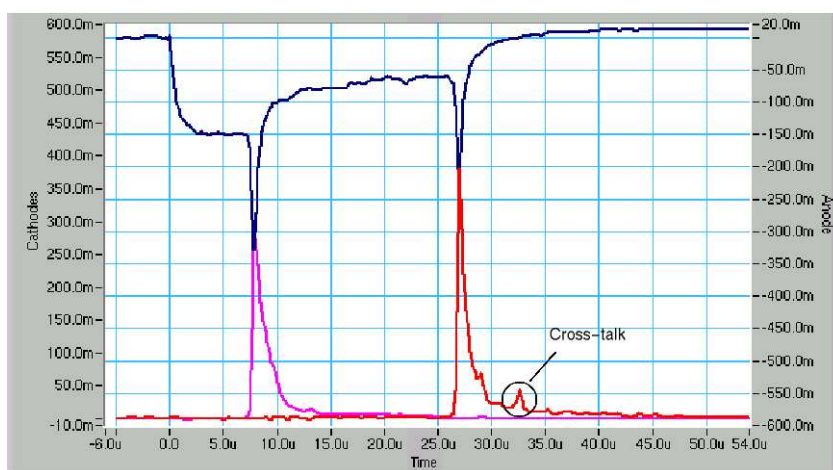


Figure 2.12: A signal from the 9-cell prototype. The anode signal (top) is blue and the cathode signals (bottom) red and pink.

# Chapter 3

## Position Reconstruction

The function of Geiger cells is to provide tracking for charged particles. The ability of these cells to correctly reconstruct the position which a particle crosses is vital. Several different methods were studied to reconstruct the times when the signal reaches the end of the cell. This chapter discusses the different methods used. Cathode signals have previously been used in NEMO-3 and this is compared to a new approach of using just anode signals.

From the anode and cathode signals 21 variables were used to characterise the anode pulse shape, such as the average voltage between the two steps and the gradient between the two steps (see Figure 2.6). Most of them were derived from the following time measurements:

1. Electron drift time ( $T_d$ );
2. Time of first anode step ( $T_{a1}$ );



3. Time of second anode step ( $T_{a2}$ );
4. Time of cathode 1 signal ( $T_{c1}$ );
5. Time of cathode 2 signal ( $T_{c2}$ ).

To find variables 1–3 from the anode signals, several methods are examined. To find variables 4 and 5, constant thresholds are applied to the cathode signals. Both the anode and cathode signals were used to measure the total propagation time. The different methods which were used to calculate the times for the anode and cathodes are:

- The NEMO-3 method using constant thresholds on the cathodes and the anode drift time.
- Using just the anode signal with constant thresholds,
- Using the anode with gradients applied to the thresholds,
- Using a differentiated anode signal with a constant threshold.

### **3.1 Methods for Reconstructing the Total Propagation Time**

The different methods used to reconstruct the total propagation time are explained in this section. The total propagation time provides a method to calculate the  $z$  resolution of the cell.

### 3.1.1 Cathode Signals

To use the cathode signals constant thresholds are set and the time is taken when the signal crosses that point. Before the signal can be used it is important to subtract the electron drift time, which corresponds to  $T_d$  as seen in Figure 3.1. The electron drift time is the time it takes for an ionised free electron to drift to the anode wire. In the NEMO-3 cells the initial ionisation corresponds to the first 10 mV drop in the anode signal [13]. This level will vary as the field strength is changed. For the purpose of these studies a level of  $\sim 10\%$  of the first flat section was used. The propagation time was obtained using the cathode signals as follows:

$$T_t = T_{c1} + T_{c2} - 2T_d , \quad (3.1)$$

where  $T_{c1}$  is the time from cathode 1 and  $T_{c2}$  is the time from cathode 2. These times were found using constant thresholds on the cathode signals. This process requires both the anode and cathode signals. It is the way in which NEMO-3 calculates propagation times.

### 3.1.2 Anode Signals with Constant Thresholds

The first method employed was the use of constant thresholds. This required two levels to be set and the times of crossing were used to determine the propagation time. Constant thresholds were applied to the anode signal. From these thresholds three times were found and are shown in Figure 3.1. From these times the total

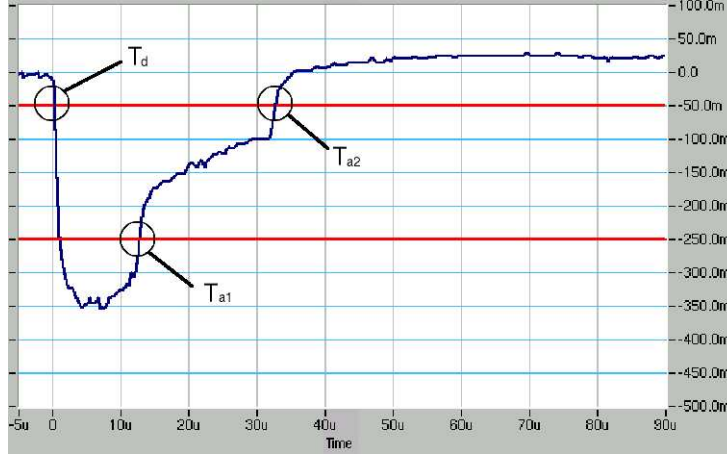


Figure 3.1: The flat thresholds used in the anode signal.

propagation time was calculated as follows:

$$T_t = T_{a1} + T_{a2} - 2T_d , \quad (3.2)$$

where  $T_t$  is the total propagation time,  $T_{a1}$  is the time from the first anode step,  $T_{a2}$  is the time from the second anode step and  $T_d$  is the electron drift time found by the upper threshold.

### 3.1.3 Anode Signals with Sloped Thresholds

To find the anode times this method used thresholds with gradients. An example of these sloped thresholds can be seen in Figure 3.2. Using this method improvements were made in correctly identifying the times on the anode signals. One of the drawbacks to the variable thresholds is that the threshold gradient used for analysing the signals needs to be fine tuned for the voltage applied to the wire. To use this method in the SuperNEMO experiment would require either complex



Figure 3.2: The use of thresholds with gradients. The anode signal is shown in blue and the lower threshold is shown in red. The dip at the start is required to improve performance for signals nearer the cell ends.

electronics or digitisation of the signals. Both of these options are not justified by the small improvement seen in comparison to using the cathode signals.

### 3.1.4 Differentiation of the Anode Signal

The third method used to examine the anode signal was the use of a differentiating algorithm. This method provides a more realistic test of the potential electronics which may be used in the final tracking chamber. There exist simple electronic circuits which can produce the same differentiating effect.

The differentiating of the digitised signal was done using a simple algorithm:

$$\frac{dy}{dx} \approx D(n) = \frac{V(n-1) - V(n)}{\Delta T} , \quad (3.3)$$

where  $\frac{dy}{dx}$  is the differentiated signal,  $V(n)$  is the voltage at the  $n$ th point of the

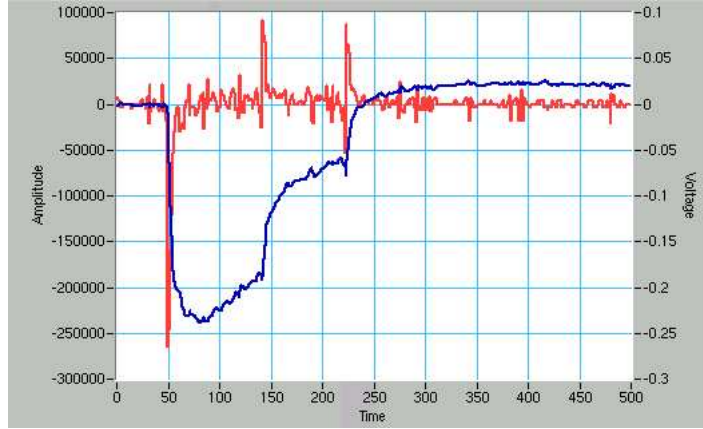


Figure 3.3: The differentiated anode signal in red and the anode signal is in blue.

digital signal,  $V(n - 1)$  is the  $(n - 1)$ th point of the signal and  $\Delta T$  is the change in time between the two points. From the differentiated signal the step times can be found using thresholds. The differentiated signal is shown in Figure 3.3. The peaks in the differentiated signal above the level of noise correspond to the pulse steps.

This method has a greater difficulty caused by the spikes from UV photons in the signals (see Figure 2.9). The UV spikes have large differentials. This results in these signals being mis-reconstructed. Their effect on the propagation time distribution can be observed in Figure 3.4. The presence of the spikes produces the “signal” which is seen with much lower propagation times. These signals are the same events which make up the tail in the cathode distributions. The difference is that these signals do not have as much of an effect on the peak of anode propagation time distribution, because they are easier to separate from the good signals. In the centre of the cell there can be additional difficulties separating the two steps when the times are so close.

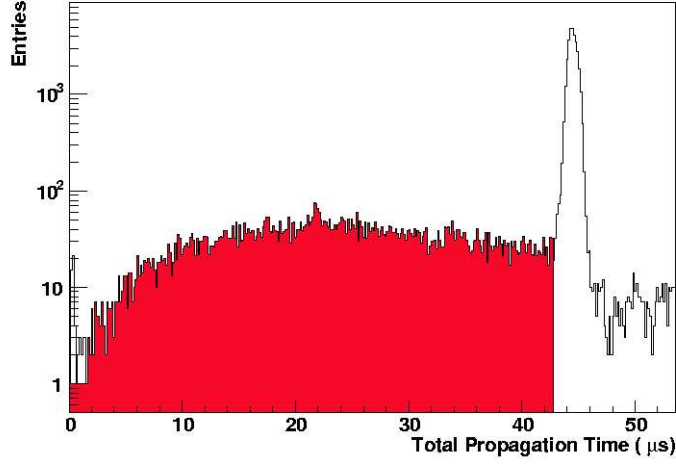


Figure 3.4: Total propagation time of the anode signal using differentiating method. The section highlighted in red comes from the UV spikes in the signals.

## 3.2 Longitudinal Position

The longitudinal hit position can be found using all of the previous methods. The following sections look at how the position is reconstructed and the effect that the method employed has on the resolution which can be obtained.

The  $z$  hit position is calculated from the total propagation time  $T_t$ . This can be determined with either the anode or cathode signals as described in Section 3.1. All methods require the electron drift time,  $T_d$ , found with a threshold on the anode signal. The times for the end of the signals can be determined using any of the four methods described in Section 3.1. The fractional hit position  $z$  is calculated using the following formula:

$$z = \frac{T_1}{T_t} \quad , \quad (3.4)$$

where  $T_1$  is the time of plasma arrival at end 1, obtained from either the anode or cathode signals, and  $T_t$  is the total propagation time which ideally should be constant, independent of  $z$ .

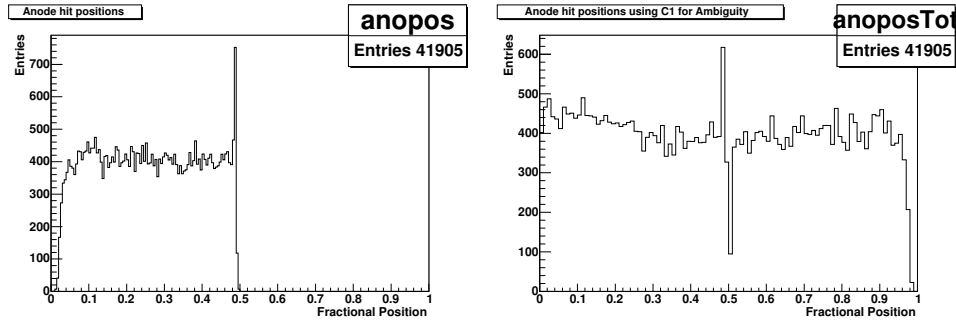
### 3.2.1 Ambiguity of the Anode Signal

One difficulty arising when using only the anode signal is an ambiguity. This ambiguity comes from the fact that it is not known which end of the cell each of the two steps originate from. Figures 3.5(a) to 3.5(c) show the distribution of hits across the length of the cell. These signals come from cosmic rays and their distribution should be random. It would be expected that all positions have the same number of hits due to the random nature.

Figure 3.5(a) is a histogram of the fractional position, defined as the position normalised to the total length, found with the anode signals. The ambiguity causes all events to be classed as from one half of the cell. It is possible to resolve this problem in most cases by using one cathode signal and finding which step in the anode signal is closest to that value. This works well for most of the wire and only has difficulties in the central region, corresponding to about 1% of the total length.

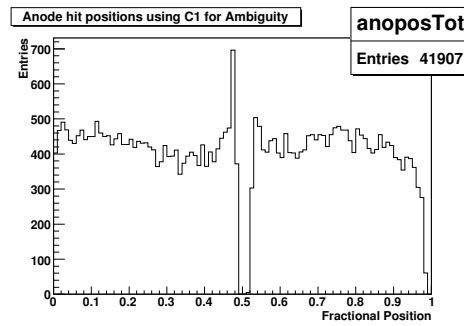
Figures 3.5(b) and 3.5(c) show the fractional position for the differentiation and constant threshold methods, respectively. Using a cathode signal to resolve the ambiguity of the signal. From the two figures the difference between using differentiation and constant thresholds methods can be seen. The largest improvement can be seen at the centre of the cell. One of the features of the differentiated sig-

nals is a better correlation with the cathode signal at all positions along the wire. This improvement means that the ambiguity can be resolved more reliably in these cases.



(a)

(b)



(c)

Figure 3.5: The number of hits per position for different methods. a) found using just the anode with the differentiation method b) using the differentiation method with one cathode signal to resolve the ambiguity c) using the constant threshold method with one cathode signal to resolve the ambiguity



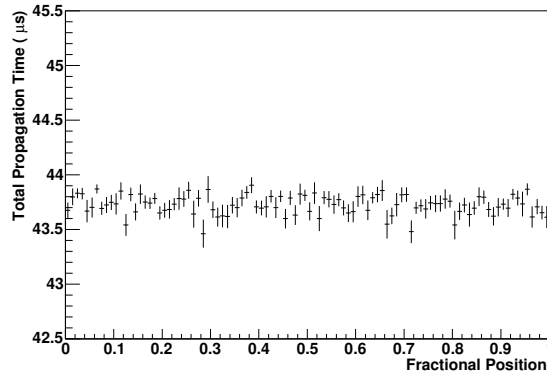


Figure 3.6: Average total propagation times for all positions along the wire reconstructed with both cathode signals.

### 3.3 Position Dependence of Total Propagation Time

With the ambiguity solved it is possible to find how the total propagation time varies on position. The total propagation time is expected to remain constant for all positions along the cell. The different methods used effect how the reconstructed total propagation time varies with position. This relates to how well the thresholds work and gives an understanding of where and why problems occur when reconstructing times.

#### 3.3.1 Cathode Signals

The cathode signals show agreement with expectation. Across the full length of the cell the the propagation time is constant. This is shown in Figure 3.6.

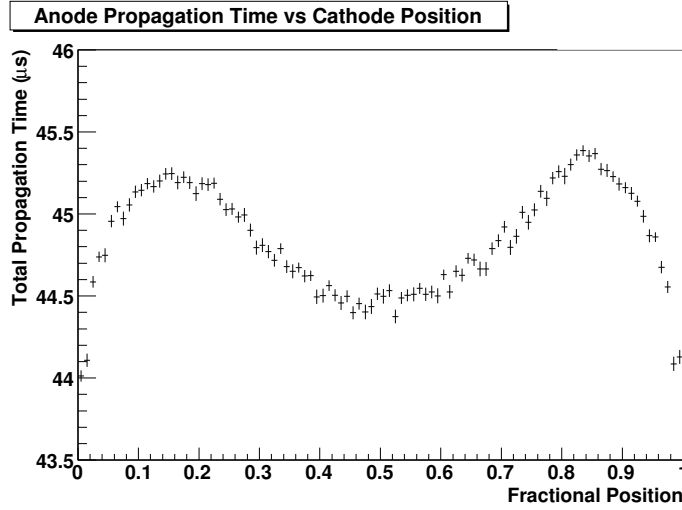


Figure 3.7: The total propagation time as a function of the fractional position is found using cathode signals. The average total propagation time found from the anode signal using constant thresholds.

### 3.3.2 Anode Signal with Constant Thresholds

The signals observed for anodes have differences in the shape depending on their point of origin along the length of the cell. This produces a dependency in the total propagation time on the position of the signal. By optimising threshold levels different positions on the wires give more consistent propagation times. Thresholds were chosen to reduce the presence of this effect. It can be observed in Figure 3.7 that there is a greater problem calculating the propagation time at the ends of the cell and at the middle. This effect arises as a result of the mistiming of the anode signal.

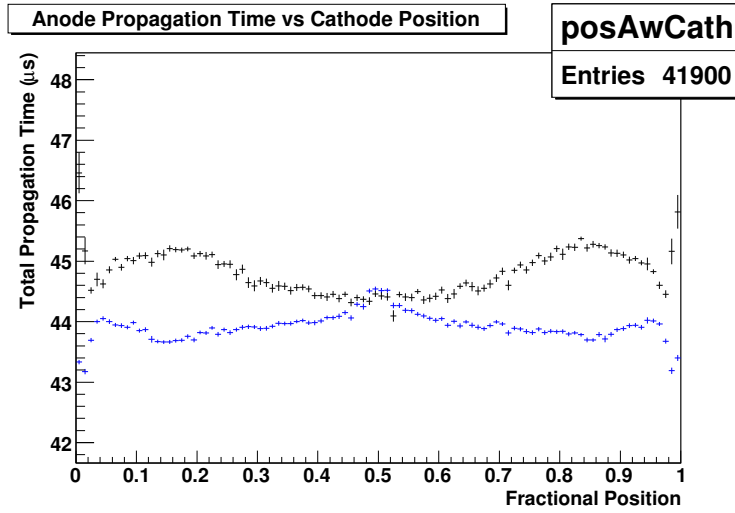


Figure 3.8: The position dependence of the average total propagation time for both flat (black) and variable thresholds (blue).

### 3.3.3 Anode Signals with Sloped Thresholds

Using the variable threshold method, small improvements were made in correctly identifying the times on the anode signals. This can be observed in Figure 3.8 which shows how the average total propagation times varies with position, for flat and variable methods. The data analysed using these variable thresholds are shown in blue while the original data are shown in black. The greatest improvement was found in the central region of the wire.

### 3.3.4 Differentiation of the Anode Signal

The differentiating method finds that the propagation time is nearly constant with position. Figure 3.9 shows the average total propagation time versus position. There are only small effects at the ends and middle of the cell. This method shows

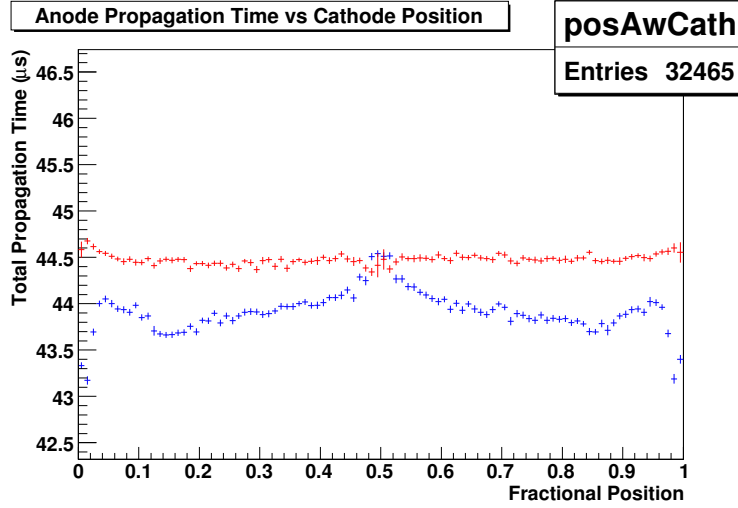


Figure 3.9: The position dependence of the average total propagation time from sloped thresholds (blue) and differentiated signal (red).

a large improvement when compared with the other two anode methods. In the central region a small deviation is observed, because it is difficult to separate the two steps when the times are close.

### 3.4 Calculating the $z$ Resolution

To study the performance of the different methods, the resolution needs to be determined. The  $z$  resolution of a Geiger cell can be calculated in two ways: using a laser or using the total propagation time.

### 3.4.1 Resolution from Laser Studies

To measure the  $z$  resolution for the NEMO-3 experiment tests were performed using a laser positioned at a specific point to excite the gas, and measuring how well the position was determined to give the resolution of the cell.

The  $z$  resolution found using the laser at different positions along the wire is shown in Figure 3.10. This measurement was made by the NEMO-3 collaboration using a 9-cell prototype. By studying how resolution varies with position for NEMO-3 the uncertainties of the time were found to scale with the square root of the propagation time ( $\sigma_{T_t} \propto \sqrt{t}$ ) [13]. This can be explained as an effect of the statistical nature in which the plasma propagates. Therefore the errors build up with the number of steps made by the UV photons. This gives a position dependent resolution of the form:

$$\sigma_z = \frac{L\sigma_{T_t}}{2T_t \sqrt{1 - \frac{4z^2}{L^2}}} = \frac{\sigma_0}{\sqrt{1 - \frac{4z^2}{L^2}}} , \quad (3.5)$$

where  $\sigma_z$  is the error in  $z$ ,  $T_t$  is the total propagation time,  $\sigma_{T_t}$  is the error in the total propagation time, found from a Gaussian fit to the distribution,  $L$  is the length of the cell and  $\sigma_0$  is the maximum resolution at the center of the cell.

### 3.4.2 Single-cell Prototype

The resolution of the single cell was measured in a different way. To find the resolution the sigma of the total propagation time was measured from a Gaussian fit.

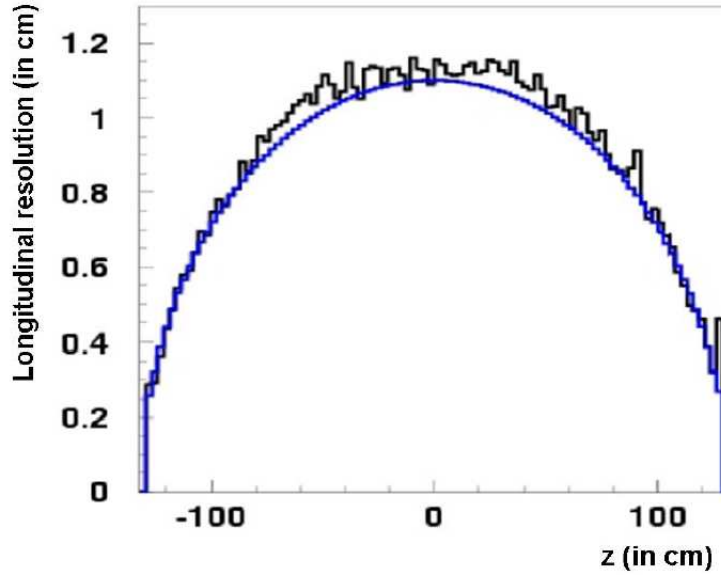


Figure 3.10: Longitudinal resolution in a NEMO-3 prototype as a function of longitudinal position, showing experimental data and the fit given by Equation 3.5 [2].

This is used because the propagation time of the plasma is expected to be constant. With the single-cell prototype the resolution was measured for different positions, instead of using hits produced by laser at known positions. The reconstructed positions are used to select the regions of the cell. The formula used to calculate the resolution of the hit position is:

$$\sigma_z = \frac{L\sigma_{T_t}}{2T_t} , \quad (3.6)$$

where  $\sigma_z$  is the  $z$  resolution,  $L$  is the length of the wire,  $\sigma_{T_t}$  is the sigma and  $T_t$  is the mean from a Gaussian fit to the total propagation time distribution. It is not possible to use the full corrected position-dependent form as there is no way to measure the position independently. The distribution found using this method therefore would not be expected to show the same relationship. The results for

this test are shown in Figure 3.11.

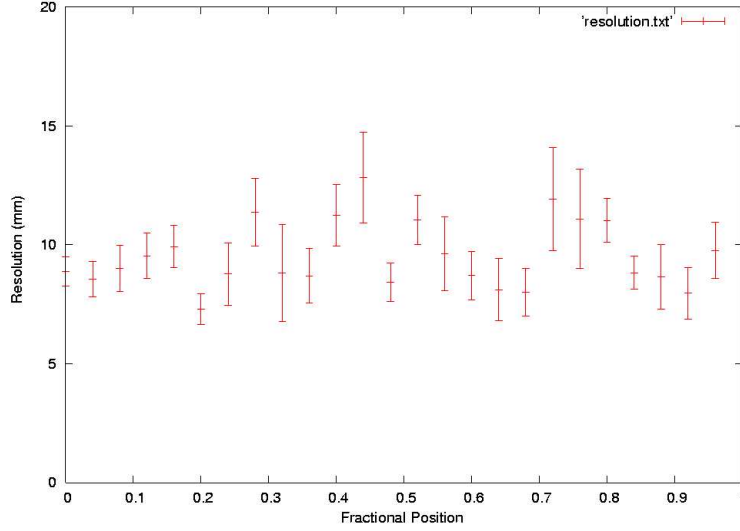


Figure 3.11: Longitudinal resolution in the single-cell prototype as a function of fractional longitudinal position. The resolution is the predicted resolution based on Equation 3.6.

From the results obtained there is no relationship between position and resolution. This result does show a disagreement with those of NEMO-3, but the difference in the methods for obtaining the resolution accounts for this discrepancy. The method used in the single cell only gives a prediction of the worst case resolution in the cell. This takes the form of a constant and so is consistent with the measurement from NEMO-3.

### 3.5 Factors Affecting $z$ Resolution

The distribution of total propagation times does not always give the intrinsic resolution of the cell. Some of the factors affecting the distribution from the anode

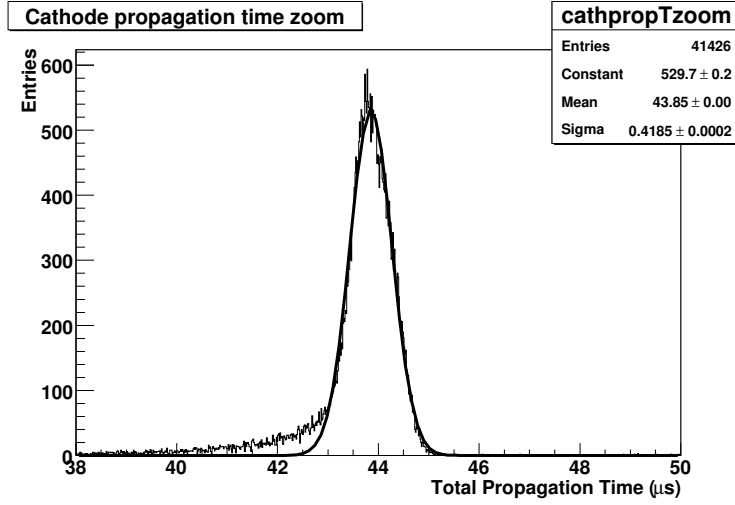


Figure 3.12: Distribution of total propagation times using times from the cathodes with a Gaussian fit.

signal relate to the threshold method used. These factors are discussed in Section 3.3.1. Other effects relate to changes in the gas properties, resulting from the changes in atmospheric pressure.

### 3.5.1 Cathode Resolution

The distribution of propagation times found is used to calculate the resolution. To find the resolution a Gaussian fit is applied to the distribution. The mean and sigma of the distribution are used in Equation 3.6  $T_t$  and  $\sigma_z$  respectively. The distribution found from the cathode signals is shown in Figure 3.12.



### 3.5.2 The Anode Resolution

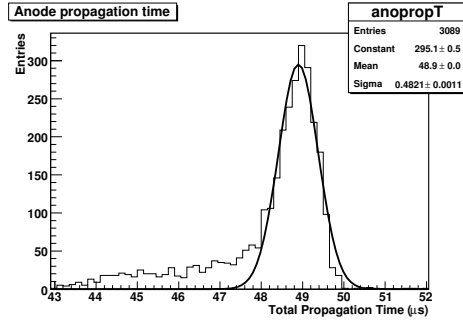
From analysis of the same data the  $z$  resolutions of the three different methods were found. A summary of the different results can be found in Table 3.1. This shows that the anode signal gives the best resolution when using the differentiating method. This method also has an improved resolution to that of the cathode method. The sloping thresholds method also shows an improvement on the constant. This is in part due to the fact that it is possible to optimise the sloped thresholds to meet when the centre of the cell is hit.

Method	$T_t$ ( $\mu s$ )	$\sigma_{T_t}$ ( $\mu s$ )	$\sigma_z$ (mm)
Cathode	43.84	0.4226	$14.56 \pm 0.06$
Constant thresholds	45.01	0.4966	$16.66 \pm 0.07$
Sloped Thresholds	44.07	0.4436	$15.20 \pm 0.08$
Differentiation	44.51	0.3923	$13.31 \pm 0.05$

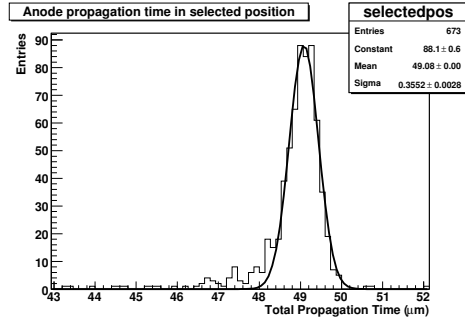
Table 3.1: Summary of the resolutions found using the four different methods. The uncertainties on  $\sigma_z$  are statistical.

Figure 3.7 shows the propagation time along the length of the wire. This effect causes the distribution of the total propagation time to be spread out. This affects the reconstructed  $z$  resolution of the cell. By using only small regions along the length of the wire, this effect is removed. The improvement in the propagation time distributions is shown in Figure 3.13. This figure shows the improvement which can be observed when selected cell positions are used with flat thresholds, in this case a fractional position of 0.15–0.25. The sigma of the two anode signals improves from  $0.48 \mu s$  to  $0.36 \mu s$ . This corresponds to an improvement of 4.0 mm in the reconstructed  $z$  resolution.

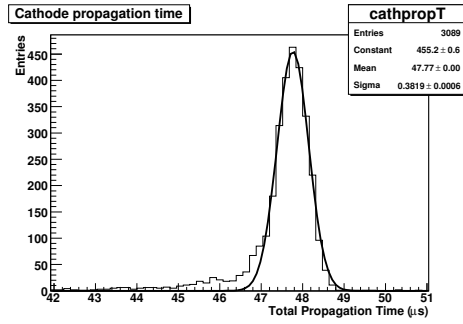
Figure 3.13 also shows the difference seen for the cathode signals. In this case



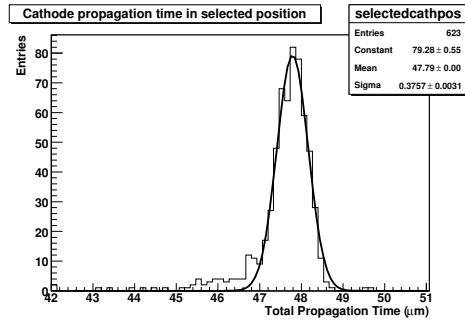
(a) Anode for all positions.



(b) Anode from selected positions.



(c) Cathode for all positions.



(d) Cathode for selected positions.

Figure 3.13: The distributions for the total propagation times from the anode (using flat thresholds) and the cathode signals.

Method	$T_t$ ( $\mu s$ )	$\sigma_{T_t}$ ( $\mu s$ )	$\sigma_z$ (mm)	Resolution Improvement (mm)
Cathode	43.83	0.4224	$14.55 \pm 0.13$	0.01
Constant thresholds	45.44	0.3444	$11.44 \pm 0.11$	5.22
Sloped Thresholds	43.98	0.3385	$11.62 \pm 0.11$	3.58
Differentiation	44.50	0.3736	$12.68 \pm 0.11$	0.63

Table 3.2: Summary of the resolutions found using the four different methods.

the difference in the sigma is negligible and the change in resolution is 0.2 mm. This demonstrates the effect of different threshold levels on the calculated anode resolution.

Table 3.2 gives the improvement that choosing a selected region has on the reconstructed resolution of the cell. The large improvement in the resolution does not work along the full length of the wire.

### 3.5.3 Atmospheric Pressure Effects

Atmospheric pressure can change quickly over short periods of time. Changes in the atmospheric pressure have been found to cause shifts in the total propagation times of the cell. Figure 3.14 shows the shift which occurs in the total propagation time during a period of two hours.

The drift effect can change the total propagation time by more than  $0.5 \mu s$  over a 30 min period. This affects the distribution of the total propagation time and therefore changes the  $z$  resolution. Data were recorded in two possible ways, either by triggering off a pair of scintillators or triggering off signals on the anode

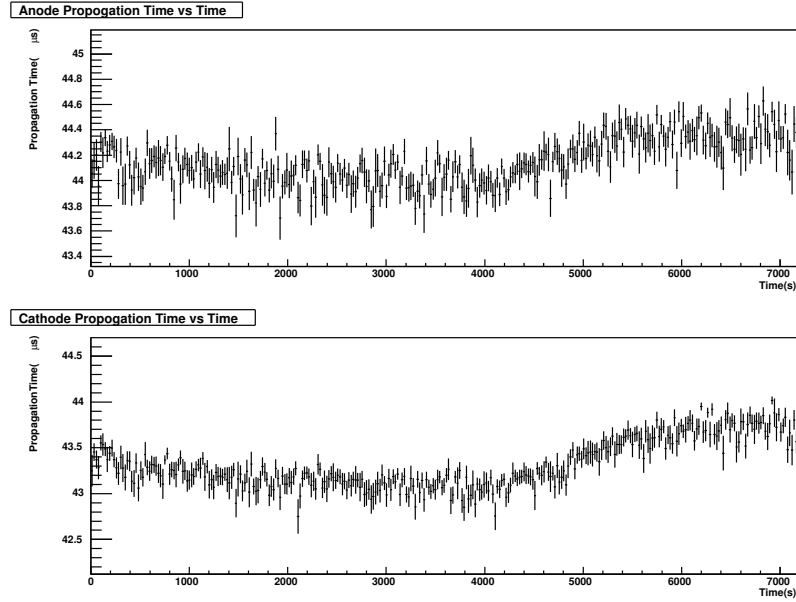


Figure 3.14: The variation of the total propagation time with time for the anode and cathode signals. The change seen occurs over a two hour period.

wire. When triggering off the scintillators, data were taken over a period of about 12 hours. The drift effect seen on these data was significant. When triggering is done from the anode signals the rate is much higher and a sufficient number of hits occur in a period of 5 to 15 minutes. Therefore the drift effect has very little effect on this data. Triggering off the anode signal allows signals to originate from all positions along the wire, not just those covered by the scintillators. This provides a better test of the different methods, and gives an improved measure of the internal resolution. Table 3.3 shows the improvement in  $z$  resolution found when reducing the time period analysed from 2 hours to 15 minutes. All methods show a significant improvement in their resolutions.

Method	Total Propagation Time ( $\mu s$ )	$\sigma_{T_t}$ ( $\mu s$ )	$\sigma_z$ (mm)	Resolution Improvement (mm)
Cathode	43.83	0.4224	$10.56 \pm 0.42$	4.00
Constant thresholds	45.44	0.3444	$14.81 \pm 0.64$	1.85
Sloped Thresholds	43.98	0.3385	$10.35 \pm 0.61$	4.85
Differentiation	44.50	0.3736	$9.39 \pm 0.29$	3.92

Table 3.3: Summary of the resolutions found using the four different methods, using data from the first 900 s.

### 3.6 Advantages of Using the Anode Signal

In section 3.5.2 it was shown that it is possible to successfully reconstruct the cell hit position using the anode signal. Measurements have been made of the resolution using different methods. These were found to give comparable resolutions to the use of the traditional cathode method. In the case of the differentiating method the resolution was found to be slightly better. The problem of ambiguity in anode signals was resolved with the use of a single cathode. The ability to use only anode signal and one cathode signal allows single-sided readout. This simplifies the cabling required as well as the costs.

### 3.7 Voltage Effects on Resolution

Changes in the operating voltage alter the point on the Geiger plateau at which the cell works. Changes would also be expected to occur as the propagation of the plasma moves from the irregular to the smooth mode discussed in Section 2.2.2. Figure 3.15 shows the change in resolution calculated at different voltages. The

resolutions from the differentiated anode methods and the NEMO-3 method in the single-cell prototype are shown.

The  $z$  resolutions which are found from both the anode and cathode methods are similar. They both show an improvement as the voltage increases and the mode of propagation becomes smoother. The upturn at the highest voltages can be explained in two possible ways. Firstly, some anode signals with UV spikes (see Section 3.1.4) are included as the method used to exclude them is not fully efficient for events which have wide spikes. Also some of the small spikes are missed. The method finds only about two thirds of all spikes. The second possible reason is that the rate of the cell is increasing and more spurious events occur. There is also a greater chance of events occurring when the field is not restored to its full strength. In this case the propagation times can become as much as double those seen at high voltages. This effect can be seen from the tail to higher propagation times and has been noted in previous research [13]. All of these effects would result in the total propagation time distribution spreading out.

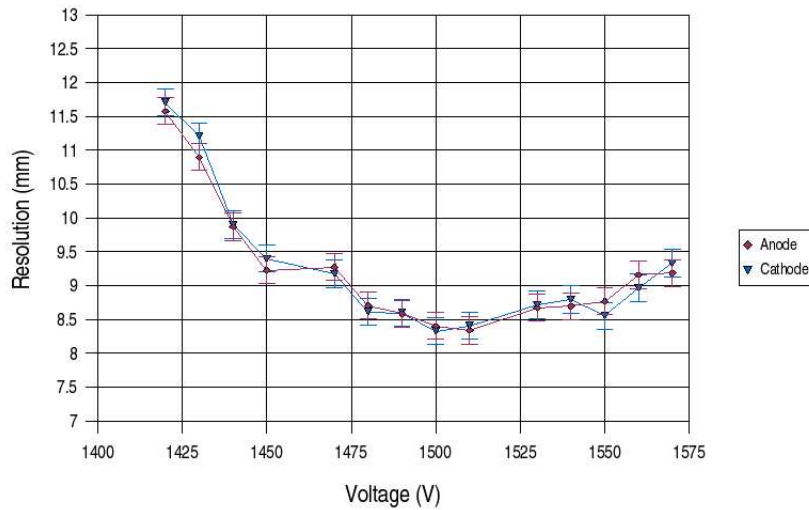


Figure 3.15: The change in resolution with voltage.

# **Chapter 4**

## **Wire Diameter Studies**

### **4.1 Introduction**

In this chapter the effects of changing the diameter of the anode wire are discussed. There are various benefits to using different wire diameters. It has been suggested that to reduce the effect of ageing the diameter of anode wires should be equal or smaller than that of cathode wires [2]. In the single cell prototype ageing was not considered. Different anode diameters were tested as smaller diameters give benefits in the tracking chamber in terms of both electrostatics and multiple scattering. Tests were performed to compare the resolution and integrated charge using wire diameters of 30, 40 and 50  $\mu\text{m}$ .

## 4.2 Simulation

It has been suggested that the Geiger plasma is dominated by ionisation produced by successive avalanches. This is related to the first Townsend coefficient [14]. A simple model was used to understand how well this process represented that seen in Geiger cells. The simulation sums the charge generated during an avalanche and calculates the number of electrons which are created during the first avalanche. The simulation uses Magboltz [15] to predict the behaviour of the gas mixture. The gas mixture used is the same as for NEMO-3: helium 94.85%, ethanol 4%, argon 1% and water 0.15%. This mixture is very close to the gas mixture used in the prototypes. The only difference is the addition of water, its effect was to improve the propagation efficiency and stabilise the cell performance.

The simulation allows the diameter of the wire and the cell size to be changed. It can be compared with data taken from the single cell prototype with different diameters of wire. It calculates two properties from the gas and the anode voltage: the electron drift time and the electron gain. The simulation was done for anode wire diameters of 30, 40 and 50  $\mu\text{m}$  and over a range of anode voltages from 1400 to 1600 V. It shows the relationship between anode voltage and the logarithm of the gain to be linear (Figure 4.1). If the simulation is correct we expect the same voltage difference between different diameters of wire at fixed gain. The difference found would be the same as that found from measurements of the integrated charge of the anode signal.



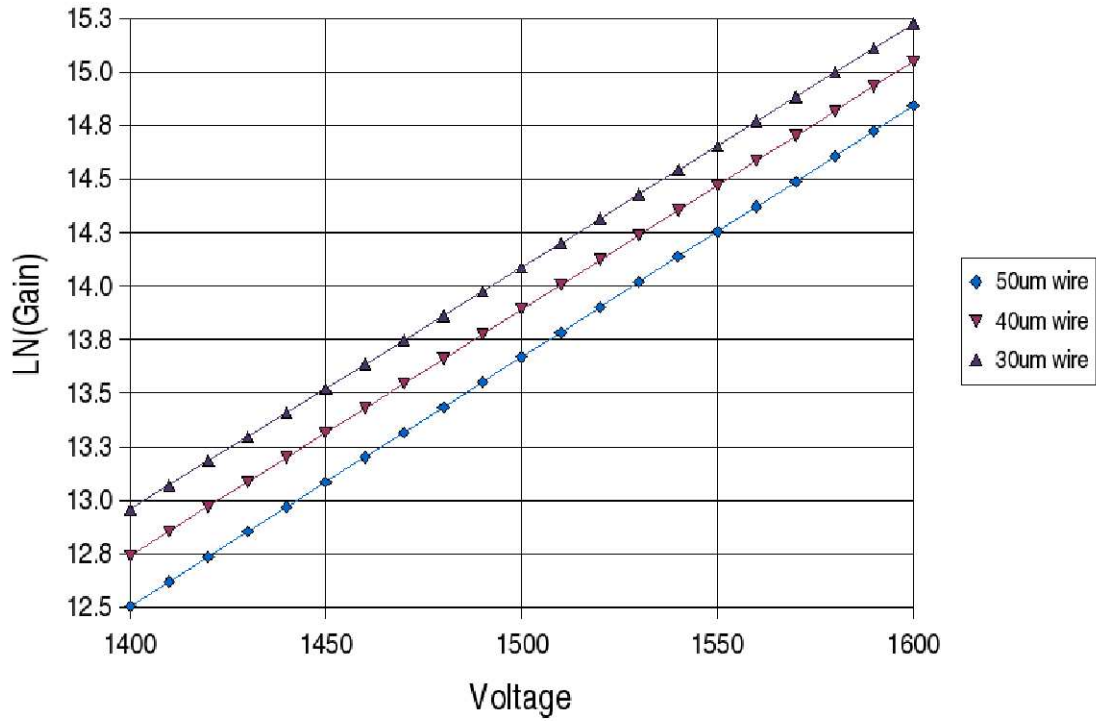


Figure 4.1: Electron gain simulated for 30, 40, and 50  $\mu\text{m}$ .

### 4.3 Single Cell Tests

The single-cell prototype was used to examine the properties of a selection of wire diameters. By understanding these properties it will help to determine the diameter of wire which is most suitable for use in SuperNEMO.

For these tests short runs of 15 minutes were used so that there was less influence from external factors. This allowed a more consistent set of data to be taken for each of the diameters used. A comparison was then made between the properties of the wires over a range of voltages.

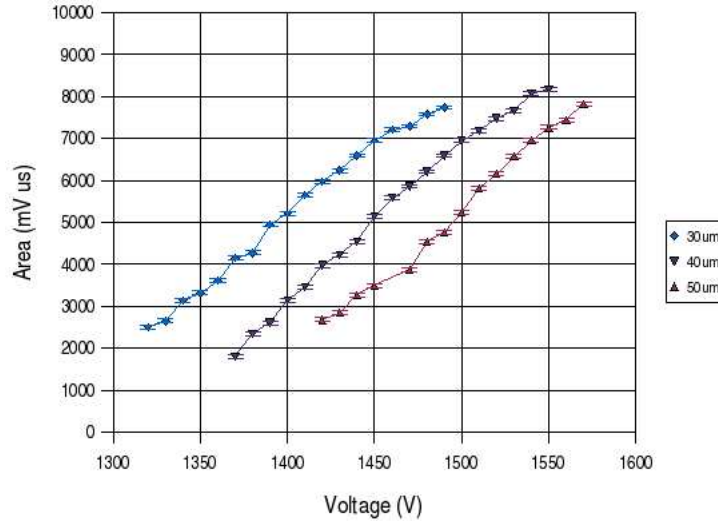


Figure 4.2: Signal area over a range of voltages with 30, 40, and 50  $\mu\text{m}$  diameter wires.

#### 4.3.1 Comparison of the Signal Area with Simulation

For comparison with simulation the area of the signals was plotted over the range of operating voltages. The area of the signal is defined as the sum of the signal voltage between  $T_d$  and  $T_{a2}$  multiplied by the difference in time between the sampling points. It is proportional to the total charge of the signal.

The best way to compare the simulation and data is to look at the difference in voltage for the same gain (from simulation) and the same area (from data). From the simulation (Figure 4.1) the expected difference was about 20 V. From the data this value was found to be about 50 V (Figure 4.2). This result is expected given the simplicity of the simulation used. The simulation does not consider the effect of the build up of positive charge on the wire. Any effect that this causes would be neglected in the simulation.

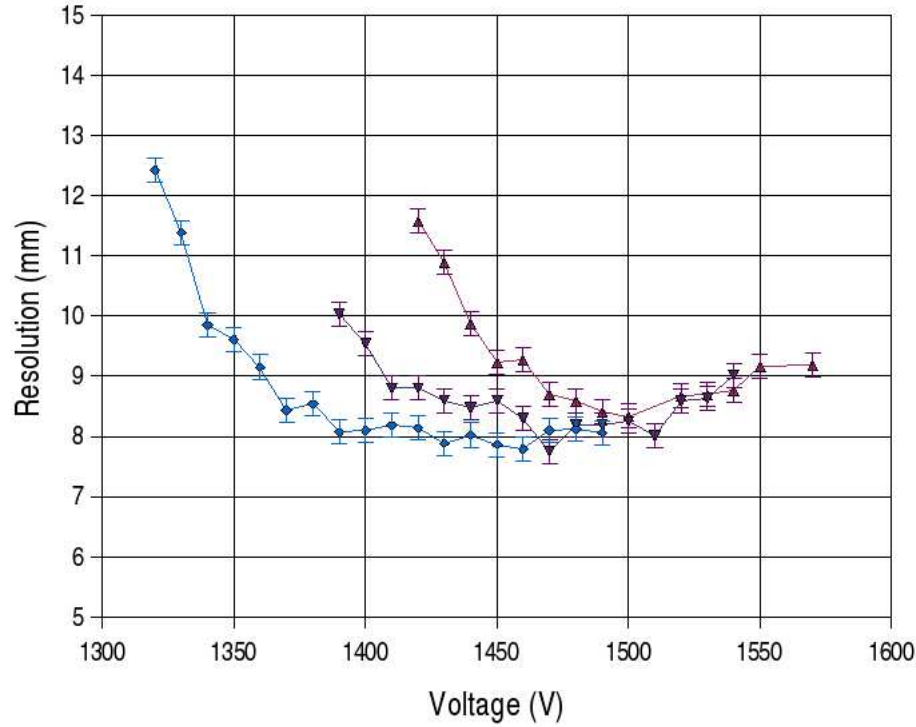


Figure 4.3: Resolution over a range of voltages with 30, 40, and 50  $\mu\text{m}$  diameter wires.

### 4.3.2 Resolution Comparison

The resolution for the three different wire diameters was measured over a range of voltages using the differentiation method. The results obtained (Figure 4.3) show that by reducing the wire diameter the resolution increases. This is a promising result as reducing the material in the tracking volume reduces the rate of multiple scattering. By averaging over the voltage range with optimum resolution for each of the diameters, resolutions of 8.0 mm, 8.3 mm and 8.7 mm were found for 30  $\mu\text{m}$ , 40  $\mu\text{m}$  and 50  $\mu\text{m}$  diameters, respectively.

## 4.4 Results

From the simulation it was expected that in moving from  $40\text{ }\mu\text{m}$  to  $50\text{ }\mu\text{m}$  there would be a shift in voltage of 20 V. When this is compared with the results from the measurements, there was found to be a larger shift in voltage. This result gives an indication that the simple nature of the simulation does not hold. Therefore, a more complex simulation is required to explain the generation of charge in a Geiger event.

## Chapter 5

### Conclusion and Discussion

The aim of this project has been to optimise the functionality of the Geiger cells. Tests were performed on a Geiger mode drift cell prototype for SuperNEMO. The tests used a single-cell prototype. Signals from the cell were recorded using oscilloscopes to digitise the pulses. These pulses were recorded to PC using a LabVIEW program. The pulse shapes were analysed and different methods were used to find the position resolution of the cell. Three different diameters of wire were compared.

Four different methods for reconstructing the hit position were compared. The anode and cathode signals were used in a traditional way, using constant thresholds and in conjunction with the electron drift time, to reconstruct the total propagation time. This method provided a baseline to compare three new anode-only methods.

The analysis of the anode pulse is a new method to calculate hit positions. The  $z$  resolutions were found using three different methods to analyse the anode signal.

These methods were compared to each other. The most effective anode method was the differentiation of anode signal. It had a constant total propagation time with  $z$  position, unlike the constant and sloped thresholds. The resolution was found to be  $(9.39 \pm 0.29)$  mm for the cathode method and  $(10.56 \pm 0.42)$  mm from the differentiation method.

The problem of ambiguity in the anode signal position was shown to be resolved with the use of a single cathode signal. Improvements in the ability to resolve the ambiguity at the central region of the cell were found to depend on the method used in analysing the anode signal. Using the constant thresholds the central 2% of the cell performed poorly. When the differentiating method was used it became less than 1%.

The resolution of the cells relates to the total propagation time. Three different methods for obtaining the total propagation time from the anode signals were compared. Each of these methods had different benefits and drawbacks. Variations in the propagation time were found to arise as a result of deficiencies in the different methods.

Tests were also performed on a selection of different wire diameters. These were compared with results from simulation. The simulation was shown not to agree with results from the single-cell prototype. The voltage shift expected from the simulation was  $\sim 20$  V, while in practice the shift was  $\sim 50$  V. The reason for this discrepancy most probably relates to the simulation ignoring the build up of charge that comes from the ions surrounding the anode wire.

The resolution for different diameter wires was found to improve slightly with

smaller diameter wires, with average values for the resolution of 7.97 mm, 8.25 mm and 8.69 mm at their peaks for 30, 40 and 50  $\mu\text{m}$ , respectively. Therefore potentially the use of 30  $\mu\text{m}$  wire would be best. However, some of the difference in resolution is due to UV spikes which affect the larger diameters more. This needs testing further in cells using ground wires to remove the presence of UV spikes.

This leads to the conclusion that for SuperNEMO it is possible to use the anode signal plus a single cathode to resolve ambiguity for finding the  $z$  position. Using this method the resolution is as good as for the cathode method and enables only one side of the detector to be cabled, helping to reduce the cost and complexity of the tracking chamber.

# **Appendix A**

## **Additional Signal Properties**

In this appendix several aspects of operating the prototypes are discussed.

### **A.1 Effects of Grounded Cathode Rings**

The use of grounded cathode rings is important to enable clear signals to be observed. Ungrounded cathodes create a charging up effect which reduces the size of the cathode signals significantly. The charging effect was most noticeable in the first few minutes of running at high voltage. In the single-cell set-up the effect reduced the signals from an average height of 40 mV to 20 mV over a period of three minutes. The effect can be seen in Figure A.1(a). The reduction in signal size makes it harder to distinguish the signals from the background noise.

By grounding the cathode rings this build up of charge does not happen. Therefore



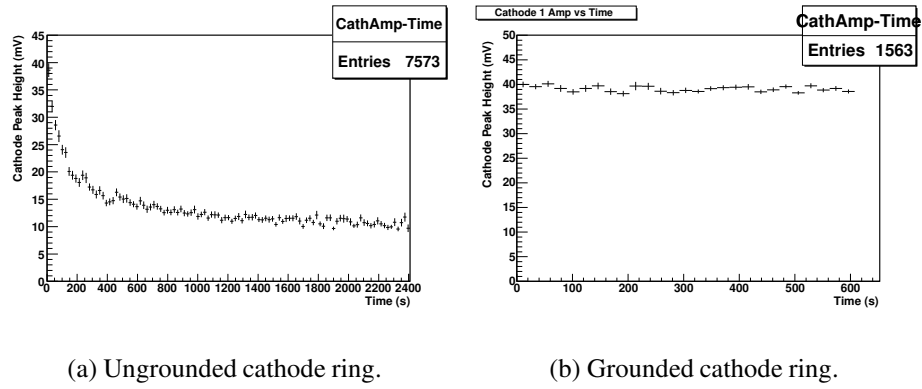


Figure A.1: The change in cathode peak height over time.

the cathode signals have the same size regardless of the length of time the cell has been running. This peak height with time for grounded cathodes is shown in Figure A.1(b).

## A.2 Cathode Peak Height with Hit Position

The peak height of the cathodes depends on the hit position in the cell. The peak height halves when comparing the height at one end to the other. This is shown in Figure A.2. The reason for this effect is not known.

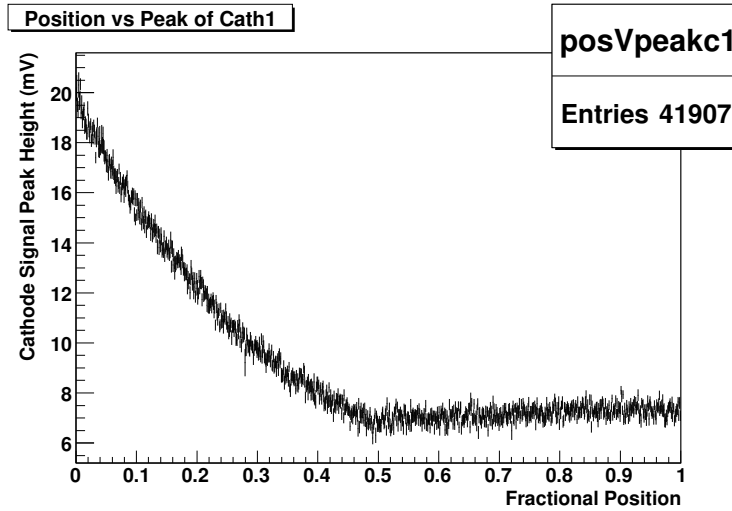


Figure A.2: The change in cathode peak height with fractional position.

### A.3 Correlation Between the Anode and Cathode Signals

The correlation between the time measured with the anode and cathode signals should be very good. Both anode and cathode measure slightly different times because the cathode signal comes when the signal enters the ring and the anode signal occurs when the signal reaches the end of the wire. Figure A.3 shows the difference for each of the three methods. The differentiated method shows a far more consistent difference in times.

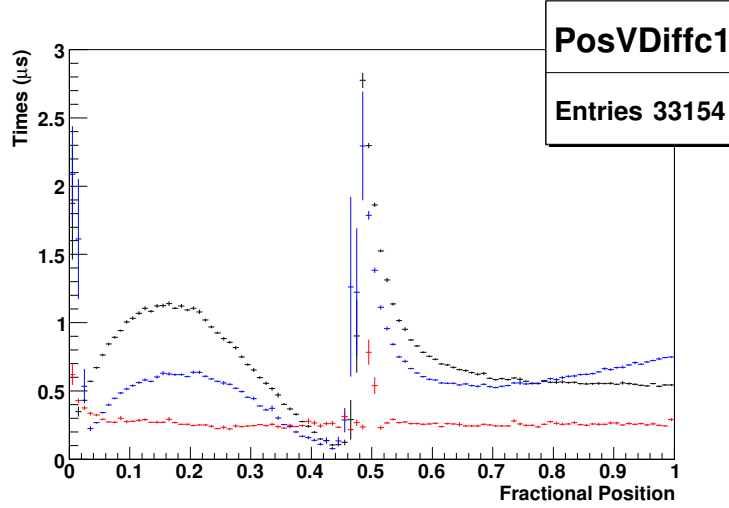


Figure A.3: The difference between anode and cathode times for the three different anode methods. The constant threshold method is in black, the sloped method is in blue and the differentiated method is in red.

## A.4 Spikes in the anode signal

The percentage of spikes for the  $50\text{ }\mu\text{m}$  wire diameter as a function of voltage is shown in Figure 2.10. Figure A.4 shows this for  $30\text{ }\mu\text{m}$ ,  $40\text{ }\mu\text{m}$  and  $50\text{ }\mu\text{m}$  wire diameters. The contribution which the spikes have is larger for larger diameter wires. While these events were removed from the analysis, not all spikes were detected as the algorithm used was not fully effective.

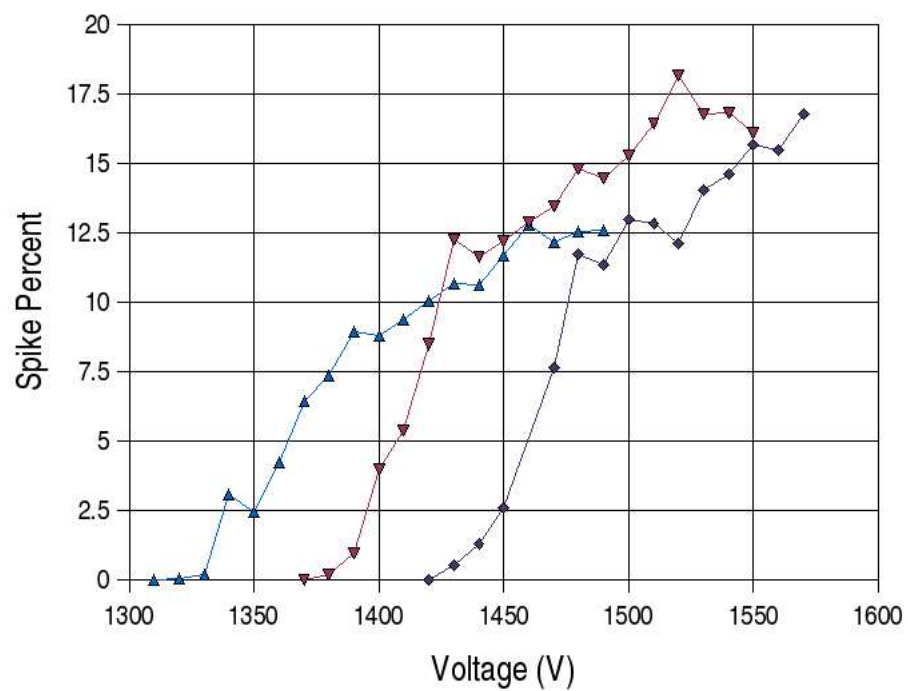


Figure A.4: The percentage of spikes over a range of voltages for anode wire diameters of 30, 40 and 50  $\mu\text{m}$ .

# Bibliography

- [1] W. Rhode et al. [HEGRA Collaboration]. Design and performance of the lead-concrete Geiger tower array within the HEGRA experiment. *Nucl. Instrum. Meth.*, **A378**:399–409, 1996.
- [2] C. Augier et al. Technical Performance of the NEMO-3 detector ”Advantages and Limitations”. LAL 05-162, 2005.
- [3] Carlo Giunti and Chung W. Kim. *Fundamentals of Neutrino Physics and Astrophysics*. Oxford, UK: Univ. Pr. 710 p, 2007.
- [4] K. Zuber. Double beta decay. *Contemp. Phys.*, **45**:491–502, 2004.
- [5] M. Goeppert-Mayer. Double beta-disintegration. *Phys. Rev.*, **48**:512–516, 1935.
- [6] W. H. Furry. On transition probabilities in double beta-disintegration. *Phys. Rev.*, **56**:1184–1193, 1939.
- [7] H. V. Klapdor-Kleingrothaus et al. Latest results from the Heidelberg-Moscow double-beta-decay experiment. *Eur. Phys. J.*, **A12**:147–154, 2001. hep-ph/0103062.

- [8] H. V. Klapdor-Kleingrothaus, I. V. Krivosheina, A. Dietz, and O. Chkvorets. Search for neutrinoless double beta decay with enriched Ge- 76 in Gran Sasso 1990-2003. *Phys. Lett.*, **B586**:198–212, 2004. hep-ph/0404088.
- [9] C. E. Aalseth et al. [IGEX Collaboration]. The IGEX Ge-76 neutrinoless double-beta decay experiment: Prospects for next generation experiments. *Phys. Rev.*, **D65**:092007, 2002. hep-ex/0202026.
- [10] Iulian Bandac. Search for neutrinoless Double Beta Decay with the CUORE detector. talk at EPS HEP, 2007.
- [11] G. F. Knoll. *Radiation Detection and Measurement*. New York, USA: John Wiley & Sons 754 p, 1989.
- [12] R. Brun and F. Rademakers. ROOT: An object oriented data analysis framework. *Nucl. Instrum. Meth.*, **A389**:81–86, 1997.
- [13] K. Errahmane. *Study of the tracking detector of the NEMO3 experiment: Simulation of the measurement of the ultra-low Tl-208 radioactivity in the source foils used as neutrinoless double beta decay emitters in the NEMO3 experiment. (In French)*. PhD thesis, Laboratoire de l’Accélérateur Linéaire, Université Paris Sud, 2001.
- [14] Denys H. Wilkinson. The Geiger discharge revisited. 1. The Charge generated. *Nucl. Instrum. Meth.*, **A321**:195–210, 1992.
- [15] S.F. Biagi. Monte Carlo simulation of electron drift and diffusion in counting gases under the influence of electric and magnetic fields. *Nucl. Instrum. Meth.*, **A421**:234–240, 1999.